

NO-A190 463

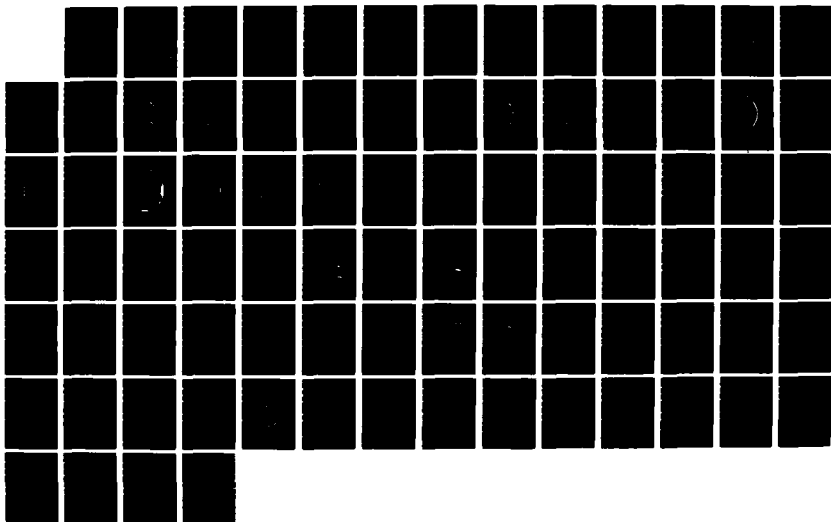
INVESTIGATION OF LASER-INDUCED PLASMA PROCESSES(U)
VISIDYNE INC BURLINGTON MA P C IP ET AL 30 DEC 86
AFGL-TR-87-0052 F19628-83-C-0149

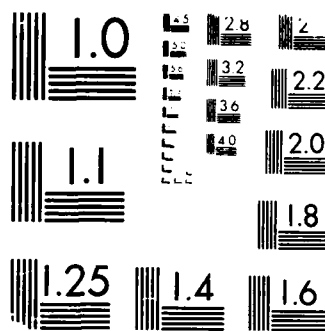
1/1

UNCLASSIFIED

F/G 00/9

NL





MICROCOPY RESOLUTION TEST CHART

NATIONAL BUREAU OF STANDARDS - 1963-A

DTIC FILE COPY

4

AFGL-TR-87-0052

INVESTIGATION OF LASER-INDUCED PLASMA PROCESSES

Precila C.F. Ip
Russell A. Armstrong

Mission Research Corporation
One Tara Blvd, Suite 302
Nashua N.H. 03062

and

James C. Baird

Brown University
Department of Physics
Providence, R.I. 02912

Prepared for:

Visidyne Corporation
10 Corporate Place
South Bedford St.
Burlington, MA 01803

30 December 1986

Scientific Report No. 14

APPROVED FOR PUBLIC RELEASE; DISTRIBUTION UNLIMITED

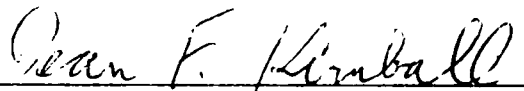
AIR FORCE GEOPHYSICS LABORATORY
AIR FORCE SYSTEMS COMMAND
UNITED STATES AIR FORCE
HANSCOM AFB, MA 01731

DTIC
SELECTED
MAR 02 1988
S E D

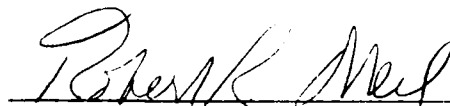
88 2 26 102

AD-A190 463

"This technical report has been reviewed and is approved for publication"

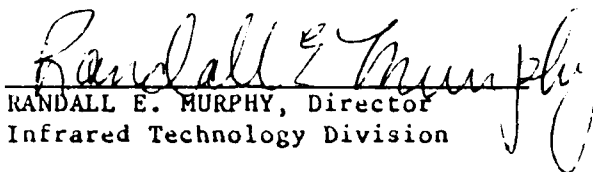


DEAN F. KIMBALL
Contract Manager
Atmospheric Backgrounds Branch
Infrared Technology Division



ROBERT R. O'NEIL, Chief
Infrared Dynamics Branch
Infrared Technology Division

FOR THE COMMANDER


RANDALL E. MURPHY, Director
Infrared Technology Division

This report has been reviewed by the ESD Public Affairs Office (PA) and is releasable to the National Technical Information Service (NTIS).

Qualified requestors may obtain additional copies from the Defense Technical Information Center. All others should apply to the National Technical Information Service.

If your address has changed, or if you wish to be removed from the mailing list, or if the addressee is no longer employed by your organization, please notify AFGL/DAA, Hanscom AFB, MA 01731. This will assist us in maintaining a current mailing list.

Do not return copies of this report unless contractual obligations or notices on a specific document requires that it be returned.

UNCLASSIFIED

SECURITY CLASSIFICATION OF THIS PAGE

REPORT DOCUMENTATION PAGE

1a REPORT SECURITY CLASSIFICATION UNCLASSIFIED		1b. RESTRICTIVE MARKING NONE	
2a SECURITY CLASSIFICATION AUTHORITY N/A		3 DISTRIBUTION/AVAILABILITY OF REPORT Approved for public release, distribution unlimited	
2b DECLASSIFICATION/DOWNGRADING SCHEDULE N/A			
4 PERFORMING ORGANIZATION REPORT NUMBER(S) MRC-NSH-R-0002		5 MONITORING ORGANIZATION REPORT NUMBER(S) AFGL-TR-87-0052	
6a NAME OF PERFORMING ORGANIZATION MISSION RESEARCH CORPORATION	6b OFFICE SYMBOL (If applicable)	7a NAME OF MONITORING ORGANIZATION AIR FORCE GEOPHYSICS LABORATORY	
6c ADDRESS (City, State, and ZIP Code) 1 TARA BLVD, SUITE 302 NASHUA, NH 03062		7b ADDRESS (City, State, and ZIP Code) HANSCOM AFB, MA 01731	
8a NAME OF FUNDING/SPONSORING ORGANIZATION VISIDYNE CORPORATION	8b OFFICE SYMBOL (If applicable)	9 PROCUREMENT INSTRUMENT IDENTIFICATION NUMBER F19628-83-C-0149	
8c ADDRESS (City, State, and ZIP Code) 10 CORPORATE PLACE SOUTH BEDFORD STREET BURLINGTON, MA 01803		10 SOURCE OF FUNDING NUMBERS	
		PROGRAM ELEMENT NO 62101F	PROJECT NO 7670
11 TITLE (Include Security Classification) INVESTIGATION OF LASER-INDUCED PLASMA PROCESSES			
12 PERSONAL AUTHOR(S) Dr. Precila C.F. Ip, Dr. Russell A. Armstrong and Dr. James C. Baird*			
13a TYPE OF REPORT Scientific No. 14	13b TIME COVERED FROM 3-14-86 TO 12-30-86	14 DATE OF REPORT (Year, Month, Day) 1986 December 30	15 PAGE COUNT 84
16 SUPPLEMENTARY NOTATION * Brown University			
17 COSATI CODES		18 SUBJECT TERMS (Continue on reverse if necessary and identify by block number)	
FIELD	GROUP	SUB-GROUP	
		1R Emissions, Oxygen Plasma, Rydberg States, Nuclear Effects	
19 ABSTRACT (Continue on reverse if necessary and identify by block number) Preliminary results on the hydrodynamics and Stark calculations of the AFGL-LINUS plasma are presented. Also reported is a kinetic analysis based on the most recent spectroscopic temperatures. Various calculations of different aspects of the LINUS plasma are shown. Finally, the codes (EXCEDE/ARTIC) which have potential applications to LARCEDE are discussed.			
20 DISTRIBUTION/AVAILABILITY OF ABSTRACT <input type="checkbox"/> UNCLASSIFIED/UNLIMITED <input checked="" type="checkbox"/> SAME AS RPT <input type="checkbox"/> DTC USERS		21 ABSTRACT SECURITY CLASSIFICATION UNCLASSIFIED	
22a NAME OF RESPONSIBLE INDIVIDUAL Dean F. Kimball		22b TELEPHONE (Include Area Code) (617) 377-3642	22c OFFICE SYMBOL AFGL/LSP

TABLE OF CONTENTS

<u>SECTION</u>		<u>PAGE</u>
I	INTRODUCTION	1
II	HYDRODYNAMICS	2
III	STARK CALCULATION	31
IV	KINETIC EFFECTS	51
V	MISCELLANEOUS ISSUES	58
VI	EXCEDE AND ARCTIC CODES	72
VII	REFERENCES	77

LIST OF FIGURES

	PAGE
Fig. 1. SALE Calculation for the Sample Case Running on the CRAY. A. Pressure B. Density C. Energy D. Speed.	4
Fig. 2. SALE Calculation for the Sample Case Running on the PC. A. Pressure B. Density C. Energy D. Speed.	8
Fig. 3. The Computing Mesh being Input into the SALE Code.	13
Fig. 4. SALE Calculation for the LINUS Case at 1 nsec. A. Pressure B. Density C. Energy D. Speed.	14
Fig. 5. SALE Calculation for the LINUS Case at 3 nsec. A. Pressure B. Density C. Energy D. Speed.	18
Fig. 6. SALE Calculation for the LINUS Case at 5 nsec. A. Pressure B. Density C. Energy D. Speed.	22
Fig. 7. Bow Tie Geometry for Laser Focal Region Illustrating Shock Wave Interaction.	30
Fig. 8. Zero Plasma Field Spectra for 18 Basis States (4d; 4f; 5d; 5f; 5g; 6d; 6f; 6g; 6h; 7f; 7g; 7h; 7i; 8f; 8g; 8h; 8i; 8j).	33
Fig. 9. OI Spectra for 18 Basis States for Electron Densities of A. 10^{16} , B. 10^{15} , and C. 10^{14} electrons/cm ³ .	39
Fig. 10. Assumed Temperature Profile for Kinetic Calculation.	54
Fig. 11. Calculated log density of species as a function of time for 10 torr oxygen.	55
Fig. 12. Calculated log density of species as a function of time for 100 torr oxygen.	56
Fig. 13. Calculation of Emission Coefficients for Free-Free Transition in the Field of an Ion.	63
Fig. 14. Front View of CVF.	65
Fig. 15. Wavelength Shift of CVF as a Function of Incident Angle.	66
Fig. 16. Wavelength Shift of CVF as a Function of Temperature.	66
Fig. 17. Optical System Using One Lens for Using CVF in LINUS.	68
Fig. 18. Optical System Using Lens, Collimator, and Slit for Using CVF in LINUS.	68

FIGURES(Continued)

PAGE

- Fig. 19. EXCEDE Calculation for the Case of 4.5 eV Incident
Electrons and 10 Collisions in N₂. 74
- Fig. 20. Radial Electron Density Profiles in LABCEDE for 4.5 eV
Incident Electrons in N₂. 75

Accession For	
NTIS GRA&I	<input checked="" type="checkbox"/>
DTIC TAB	<input type="checkbox"/>
Unannounced	<input type="checkbox"/>
Justification	
By	
Distribution/	
Availability Codes	
Dist	Avail and/or Special
A-1	



TABLES

	PAGE
Table 1. Comparison of Shock Front Velocity Calculated from SALE and from Blast Wave Theory.	26
Table 2. Reaction Set for LINUS Recombination	52
Table 3. Spectroscopic Temperatures for Oxygen in LINUS	53

I. INTRODUCTION

This final report summarizes work performed during the period March 1986-December 1986 under Visidyne contract No. F19628-83-C-0149, MRC work order 15105 WPR.

The purpose of the study is to investigate properties of the laser-induced plasma in the LINUS experiment in order to test its validity as a benchmark source for a plasma plume model and as a basis for more sophisticated model development. Plasma recombination processes are responsible for the large amount of radiation (ultraviolet, visible, and infrared) generated in a plasma initiated by a laser beam. The spectral information gained and the processes responsible for their generation are important in their potential application to understanding the spectral emission arising from an actual nuclear airburst. The results may be benchmarked against Sappenfield's plasma radiance model[1] which has been extrapolated to the infrared regime where there is little data available. However, before any comparison can be made, we must first complete a full detailed analysis of the laser-induced plasma.

Section II discusses the hydrodynamics in LINUS. Section III presents a Stark calculation for application to analysis of LINUS. Section IV deals with the kinetic effects and Section V shows the calculations of various important issues in LINUS.

Section VI discusses the Excede and Arctic codes which are important in their application to LABCEDE, a LINUS-related low density plasma project. The LABCEDE experiment employs an electron beam to excite atmospheric gases the purpose of which is to validate and develop atmospheric weapons effects codes. The Arctic code calculates radiance arising from electron excitation of atmospheric gases in an aurora and may be useful in the analysis of linear and non-linear effects in LABCEDE. The primary interest in relating LINUS and LABCEDE is that atomic oxygen emissions seen in LABCEDE have some common characteristics with those in LINUS[2].

II. HYDRODYNAMICS IN LINUS

A. INTRODUCTION

This section summarizes the preliminary investigation into the dynamics of the discharge region in the LINUS experiment. The hydrodynamics study is important for understanding the general morphology of the plasma expansion and the effects on recombination and radiative properties. Furthermore, gradient profiles of electron density and temperature are required to characterize the laser induced plasma. The important hydrodynamical processes to be examined are the generation of shock fronts and initial expansion due to laser energy deposition, shock front effects, post-shock cooling, and pressure recovery.

We have initiated the calculations of the shock front and expansion characteristics assuming simple ordinary fluid dynamics. The code which is used for this purpose is the Simplified Arbitrary Lagrangian Eulerian (SALE) code originally written by Amsden et al.[3] from Los Alamos Scientific Lab (now LANL). SALE is a general fluid code which uses a simplified numerical fluid dynamics computing technique to calculate two-dimensional fluid flows. It can handle flow speed from the incompressible to the supersonic limit in the Lagrangian or the Eulerian mode, or anywhere in between. In the Lagrangian mode, the cell vertices move with the fluid whereas in the Eulerian mode, the grid vertices remain stationary with respect to the fluid. The code has been widely used and well tested. Its major limitations for the present application are the treatment of only one species and no allowance (yet) for energy loss.

The code is based on the solution to the Navier-Stokes fluid equation of motion and the mass and internal energy equations. One begins by specifying the geometry of the computing mesh which is a set of quadrilateral cells. For each cell, the code calculates momentum, position, volume, energy, mass density, and pressure. The pressure is calculated from the specified equation of state. Input variables are the initial time step, the initial density and specific internal energy. All subsequent time steps are automatically adjusted. The code calculates all the above parameters for every cell and each time step until it comes to the terminating time (input by user).

B. RUNNING ON THE PC

The code resides on the Los Alamos Cray computer. We have been able to convert the code to run on the PC. The Cray is about 160 times faster than the PC but to run a job is considerably more expensive and less accessible. The SALE code is about 2000 lines and the executable image is about 340K bytes which is well within the memory buffer (640K) of the PC.

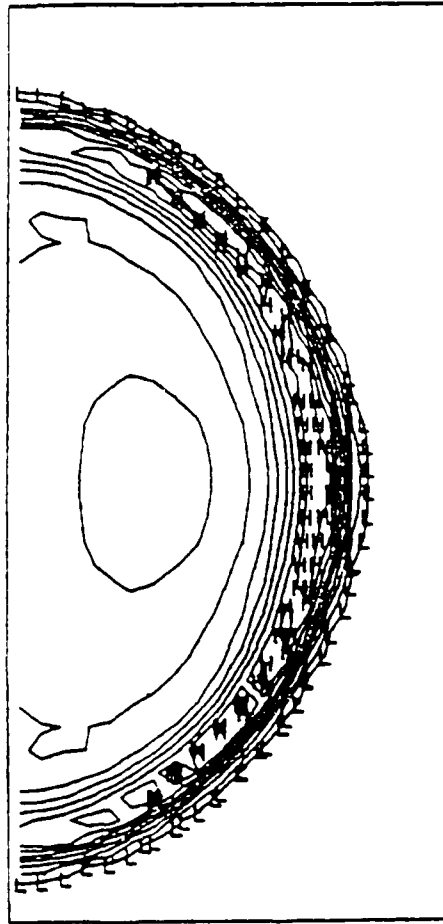
In the test case the initial parameters are $\sim 1 \mu\text{J}$ of energy deposited into a focal region of $50 \mu\text{m}$ by $120 \mu\text{m}$. Although the initial test energy was lower than that in LINUS, the morphological results should be similar. This sample case was run on both the CRAY and the PC. The results are identical except for differences which have been attributed to round off effects. These calculations are shown in Figs. 1 and 2 which represent contour plots of pressure, density, energy, and speed. The time it takes to run this particular sample case is 30 seconds on the CRAY and 1.25 hours on the PC.

C. APPLICATION TO LINUS

1. Initial Parameters

Historically[4,5,6], the focal length of the lens used in the experiment has been reported to be 5.6 to 5.8 cm and the laser power absorbed is $\sim 10\%$. Recent measurements in a new configuration[7] show that the focal length is 4.1 cm and the laser power absorbed is $\sim 40\%$. Since the calculation shown here precedes the new determination, the numbers used are all based on the earlier measurement.

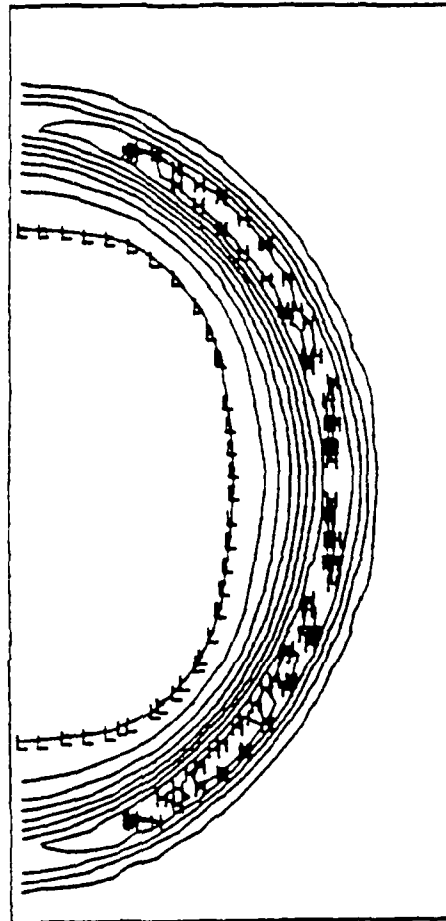
The dimension of the focal region where the laser energy is deposited is calculated from the focusing lens formula (see Section V.B). With a 5.8 cm focal length lens, it results in a focal radius of $15 \mu\text{m}$ and length of focal region of $110 \mu\text{m}$. The measured initial laser energy is 1 J but the use of 100 mJ and greater energy input to the code resulted in an error during runtime which still waits to be resolved. However, the code runs successfully when the energy input is reduced to 10 mJ. Therefore, the amount of energy deposited used in the calculation is taken to be 10 mJ and is assumed to be uniform and instantaneous. The energy deposited is entered as a multiplier of the initial specific internal energy. All the units in the code are in the cgs system.



PRESSURE
(dyne/cm²)

EXPORT-SA 09/29/88 12:46:40 TEST C E
 ISOBARS MIN- 1.99980E+05 MAX- 2.83803E+06 L- 4.73785E+05 H- 2.86423E+06 DO- 2.73805E+05

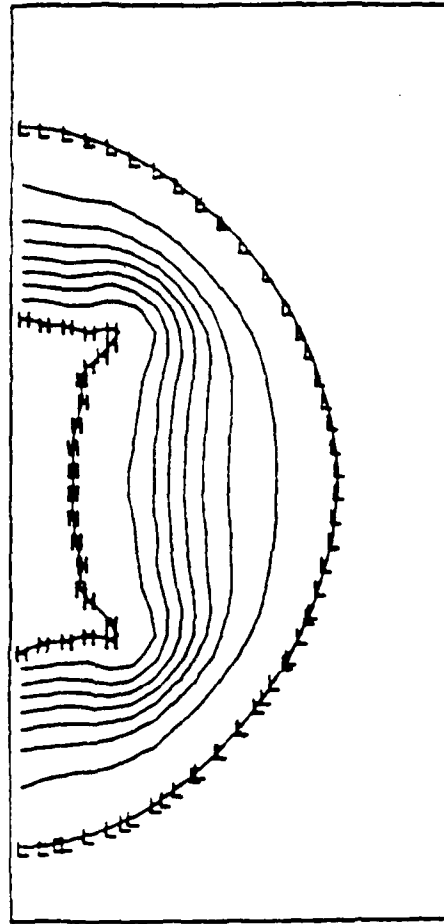
Fig. 1A. SALE Calculation for the Sample Case
Running on the CRAY.



DENSITY
(g/cm³)

EXPORT-SA 09/29/88 12:48:40 TEST C E
 ISONYCNICS MIN- 7.87356E-08 MAX- 2.18843E-04 L- 2.90705E-05 H- 1.98846E-04 DO- 2.11889E-05

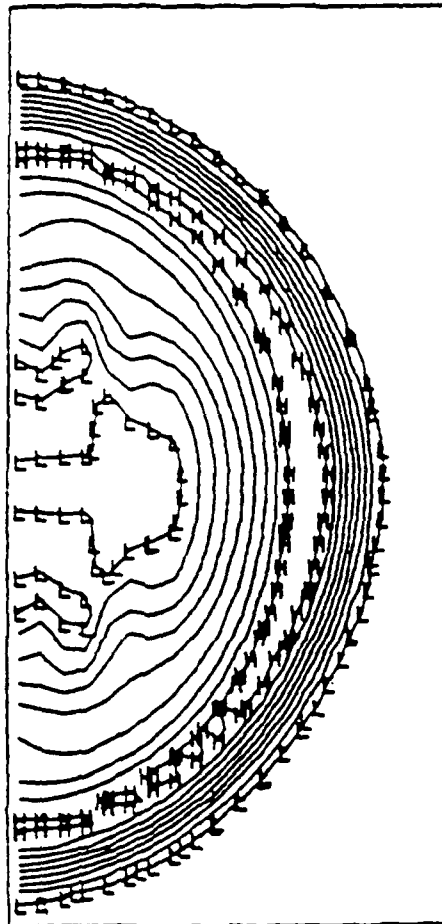
Fig. 18. SALE Calculation for the Sample Case
Running on the CRAY.



ENERGY
(erg/g)

EXPORT-9M 09/29/88 12:48:40 TEST C F
ISOTHERMS MIN= 3.00000E+09 MAX= 1.53270E+11 L= 1.80270E+10 H= 1.38243E+11 DO= 1.50270E+10

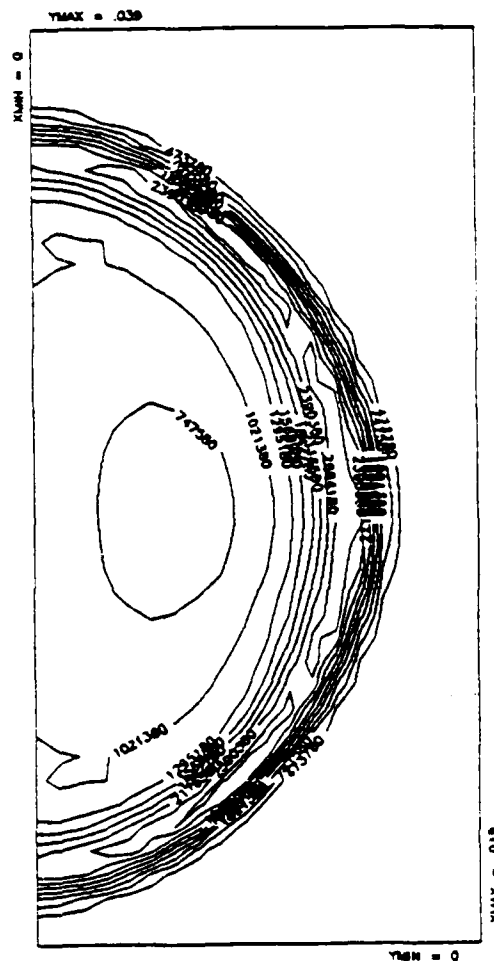
Fig. 1C. SALE Calculation for the Sample Case
Running on the CRAY.



SPEED
(cm/sec)

EXPORT-SA 09/29/88 12:48:40 TEST C E
 SPEED MIN= 2.91385E-10 MAX= 1.80973E-05 L= 1.60873E-04 H= 1.44875E-05 DO= 1.80973E-04

Fig. 1D. SALE Calculation for the Sample Case
Running on the CRAY.



ISOBARS - TEST CASE

Fig. 2A. SALE Calculation for the Sample Case
Running on the PC.

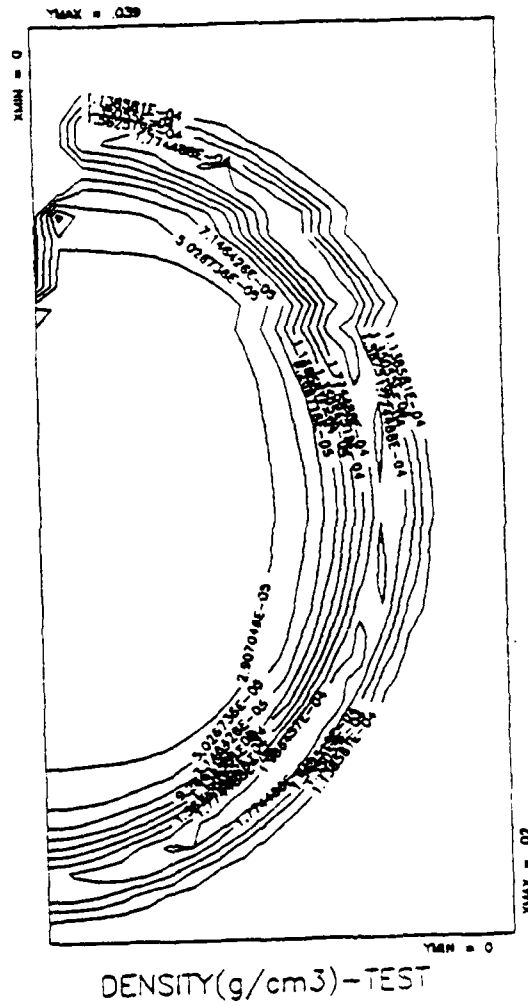


Fig. 2B. SALE Calculation for the Sample Case
Running on the PC.

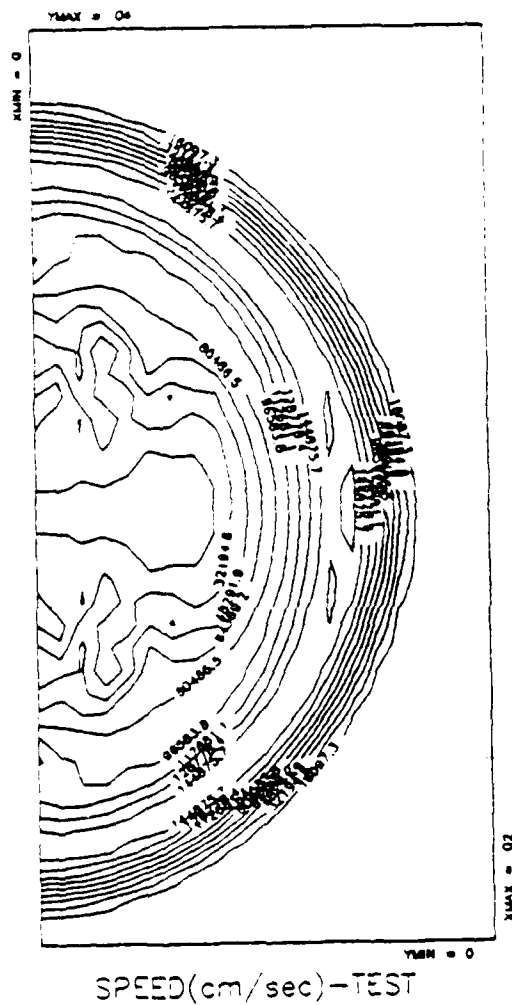


Fig. 2D. SALE Calculation for the Sample Case
Running on the PC.

Using the ideal gas law with an initial pressure of 150 torr of oxygen gas at room temperature, the initial mass density is $2.4 \times 10^{-4} \text{ g/cm}^3$. The ideal gas equation of state is assumed throughout the calculation.

The computing mesh in cylindrical coordinates is shown in Fig. 3. This is a 20×40 grid with each cell defined by a $10 \text{ } \mu\text{m}$ square. The laser propagation axis is the left boundary which is also the symmetry axis in the cylindrical coordinates. Laser energy of 10 mJ is deposited into a focal region of $10 \text{ } \mu\text{m}$ by $120 \text{ } \mu\text{m}$. An implicit Eulerian calculation is performed up to 5 nsec.

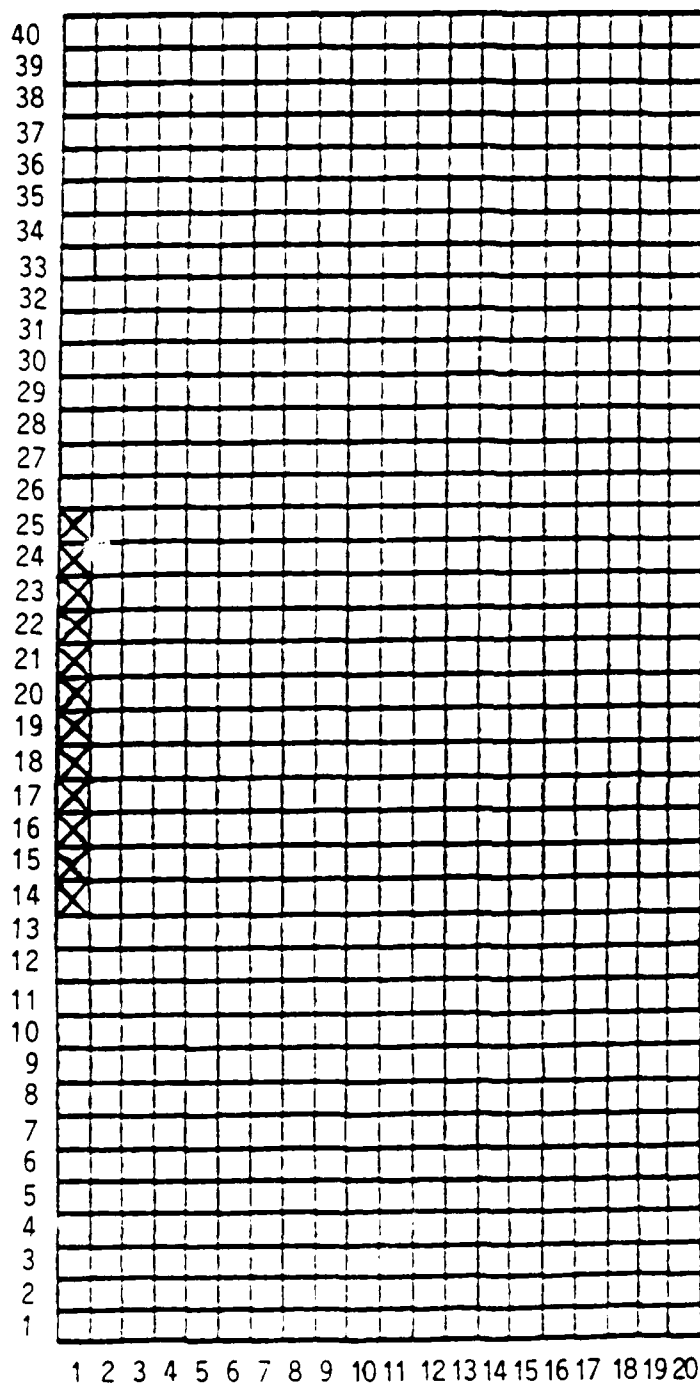
2. Results

Figs. 4, 5, and 6 show the results of the calculation at 1, 3, and 5 nsec respectively. One can clearly see the plasma expansion and the shock front propagation as time proceeds. The initial region for energy deposited is cigar-shaped and it quickly expands spherically to 0.4 mm in less than 5 nsec, thus the full size of the spark (2 mm) may be reached in ~20 nsec. This implies that it may not be feasible to use the optical multi-channel analyzer (OMA), which has a 30 nsec time resolution, to study the expansion behavior of the plasma.

The density plots show a drop of about an order of magnitude in the core region. This means that the effect of the laser energy deposition is to rapidly sweep the gas outward, as one intuitively expects. In addition, the figures show that the shock front velocity is on the order of 10^6 cm/sec . This may be compared to values obtained by other researchers. Wilke[8] reported a value of $5.7 \times 10^5 \text{ cm/sec}$ in 50 torr air. Askar'yan[9] gave a value of 10^6 cm/sec . Laser/foil target plasma experiments in NRL[10] measured a value of $3 \times 10^7 \text{ cm/sec}$ in 15 mTorr H_2 with 10 J of laser energy, although this experiment was with a solid target implying different energy accommodation. The value presently calculated is thus very close to previously reported numbers. The velocity of sound under the initial conditions is about $4 \times 10^7 \text{ cm/sec}$.

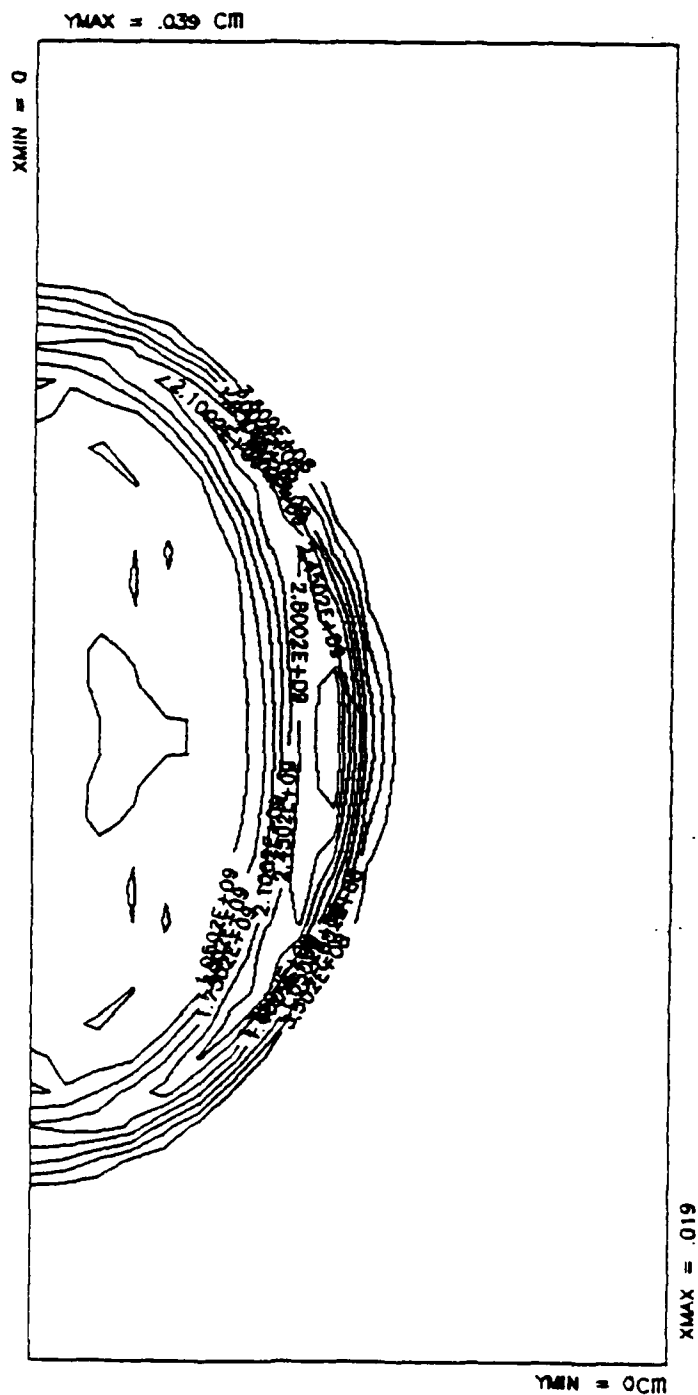
Blast wave theory[11] gives a formula which relates the shock front velocity to the pressure behind shock, which is

$$p_s = \frac{2}{\gamma+1} \rho_0 \left(\frac{dr}{dt} \right)^2$$



20x40 cells
10 μ x 10 μ per cell
ENERGY DEPOSITED=10mJ
FOCAL REGION=10 μ x120 μ

Fig. 3 The Computing Mesh being Input into the SALE Code.



ISOBARS T=1NS

Fig. 4A. SALE Calculation for the LINUS Case at 1 nsec.

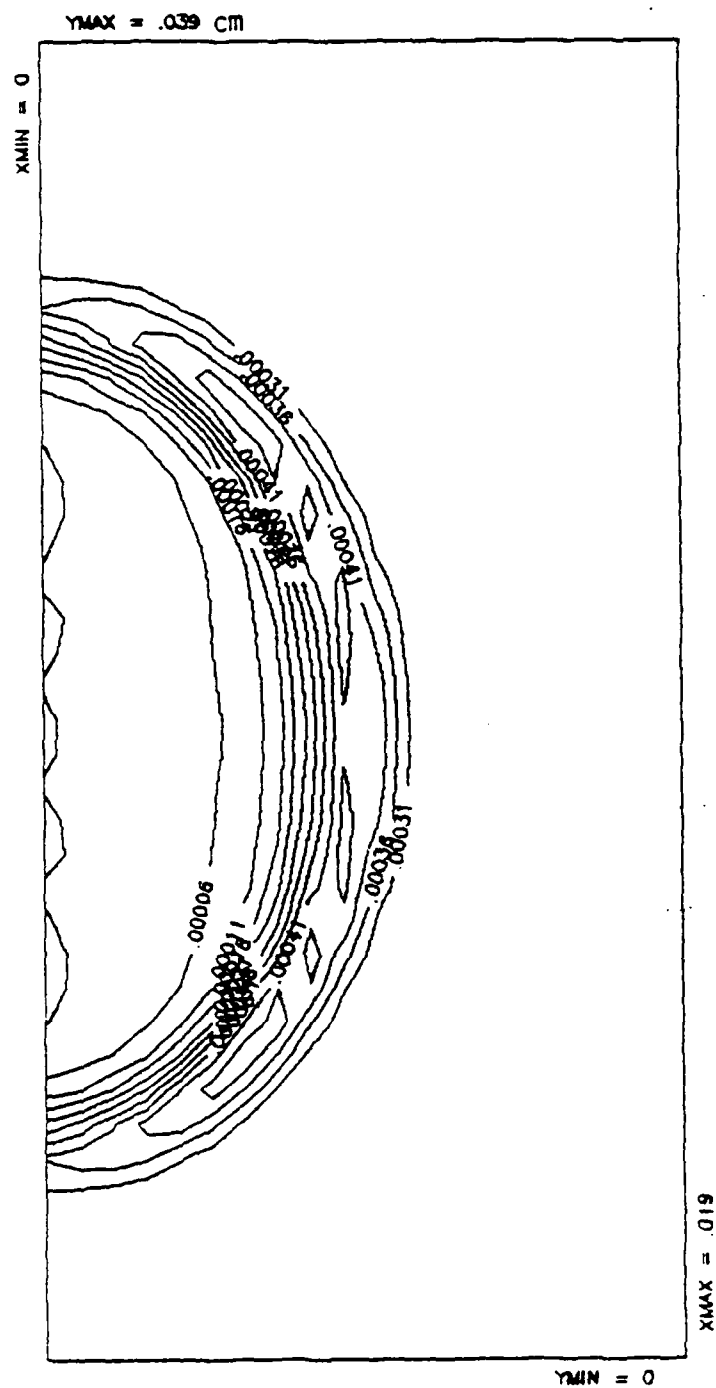
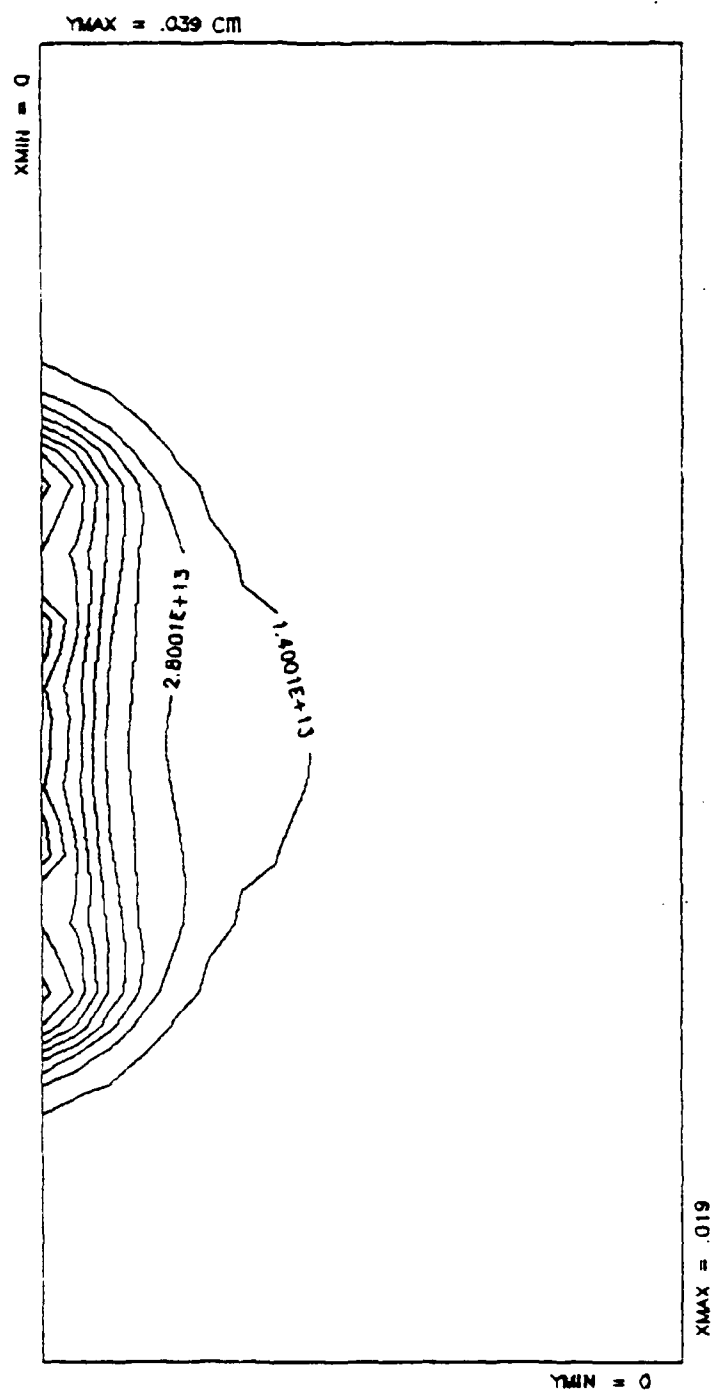
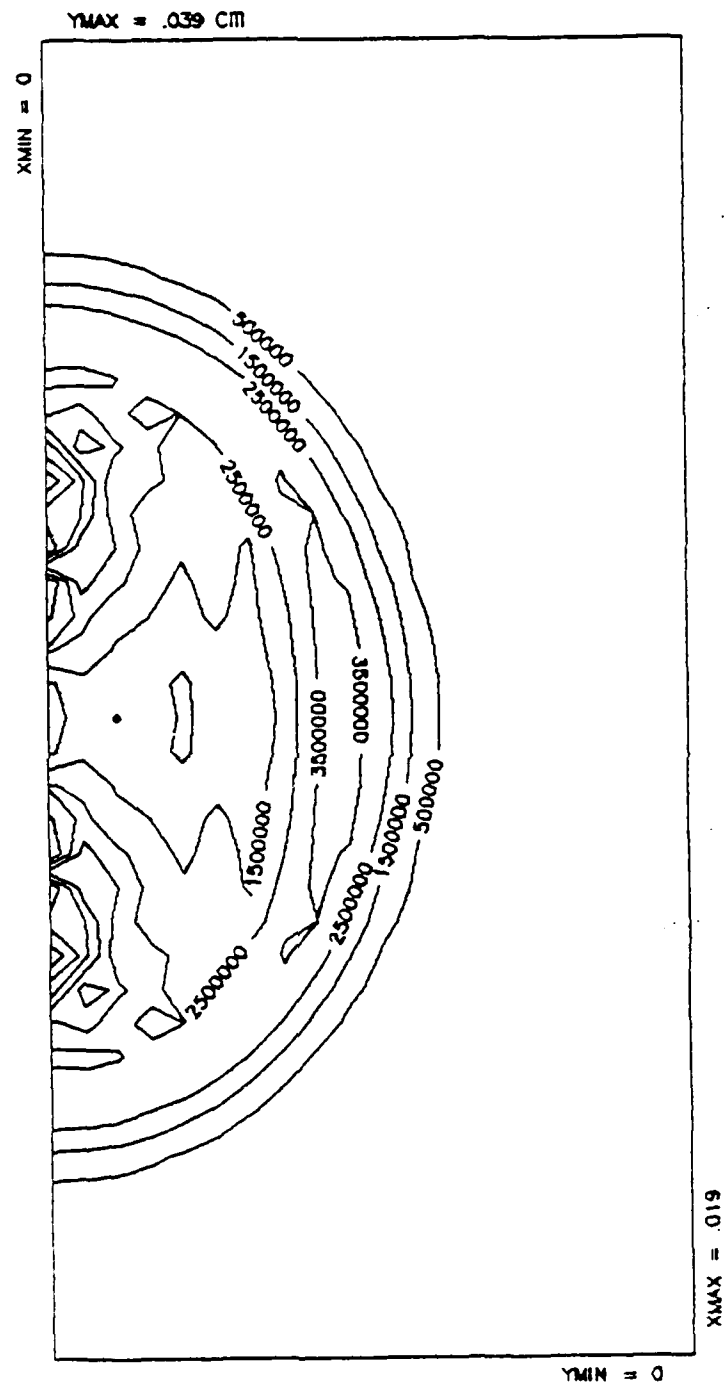


Fig. 4B. SALE Calculation for the LINUS Case at 1 nsec.



ENERGY(erg/g) T=1NS

Fig. 4C. SALE Calculation for the LINUS Case at 1 nsec.

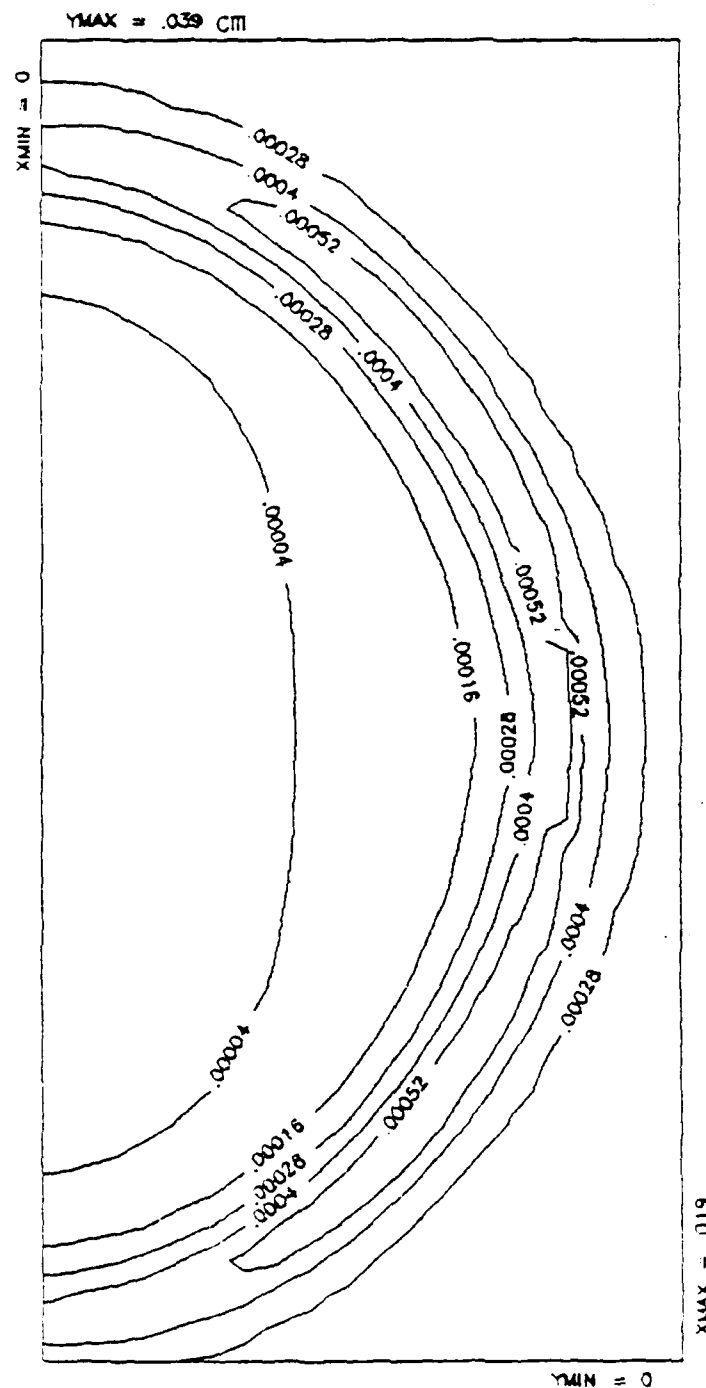


SPEED(cm/sec) T=1NS

Fig. 4D. SALE Calculation for the LINUS Case at 1 nsec.



18



DENSITY(g/cm³) T=3NS

Fig. 5B. SALE Calculation for the LINUS Case at 3 nsec.

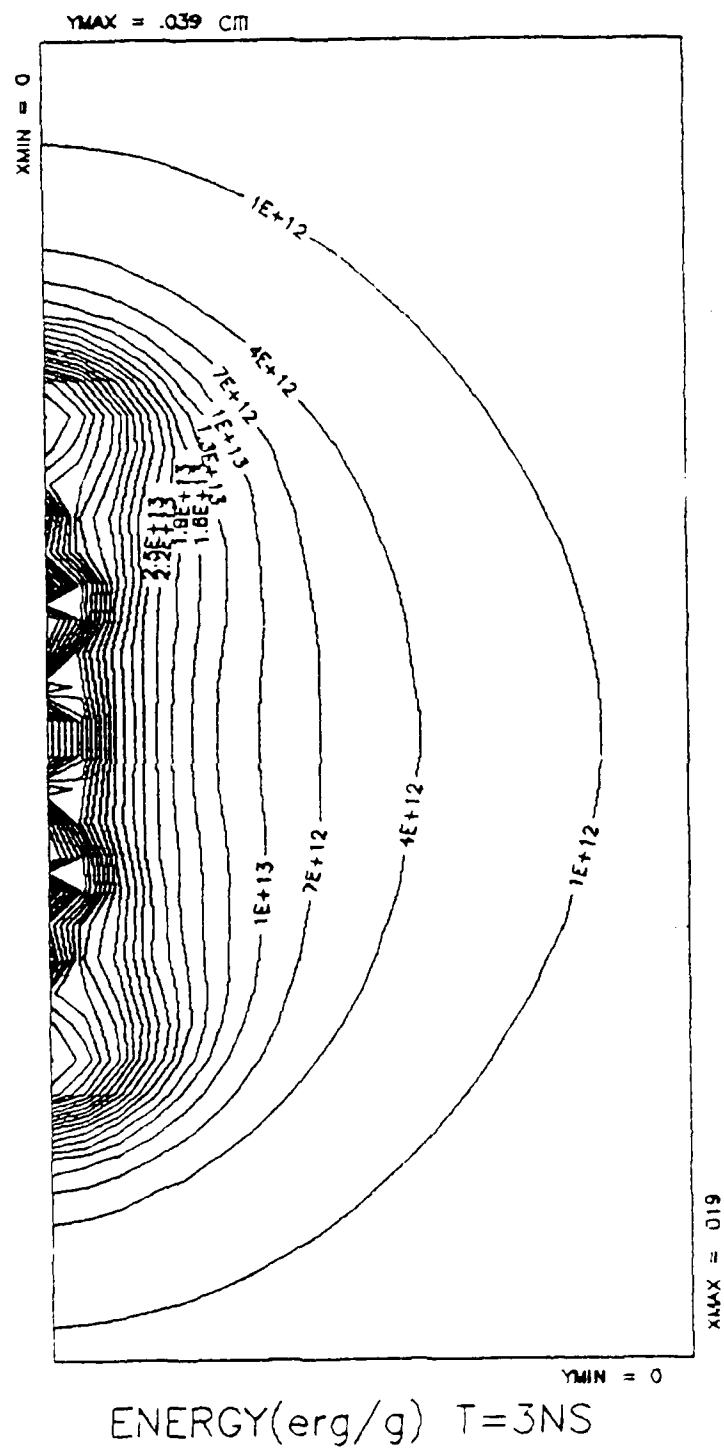
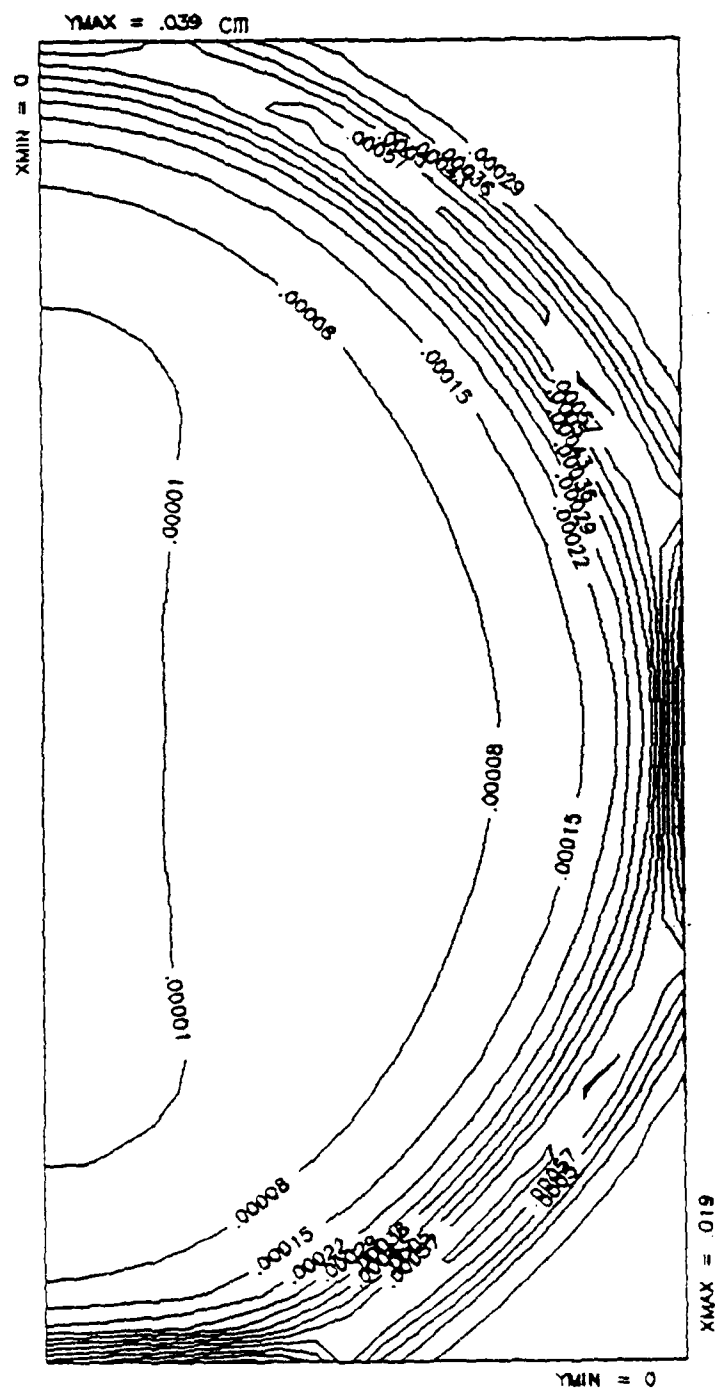
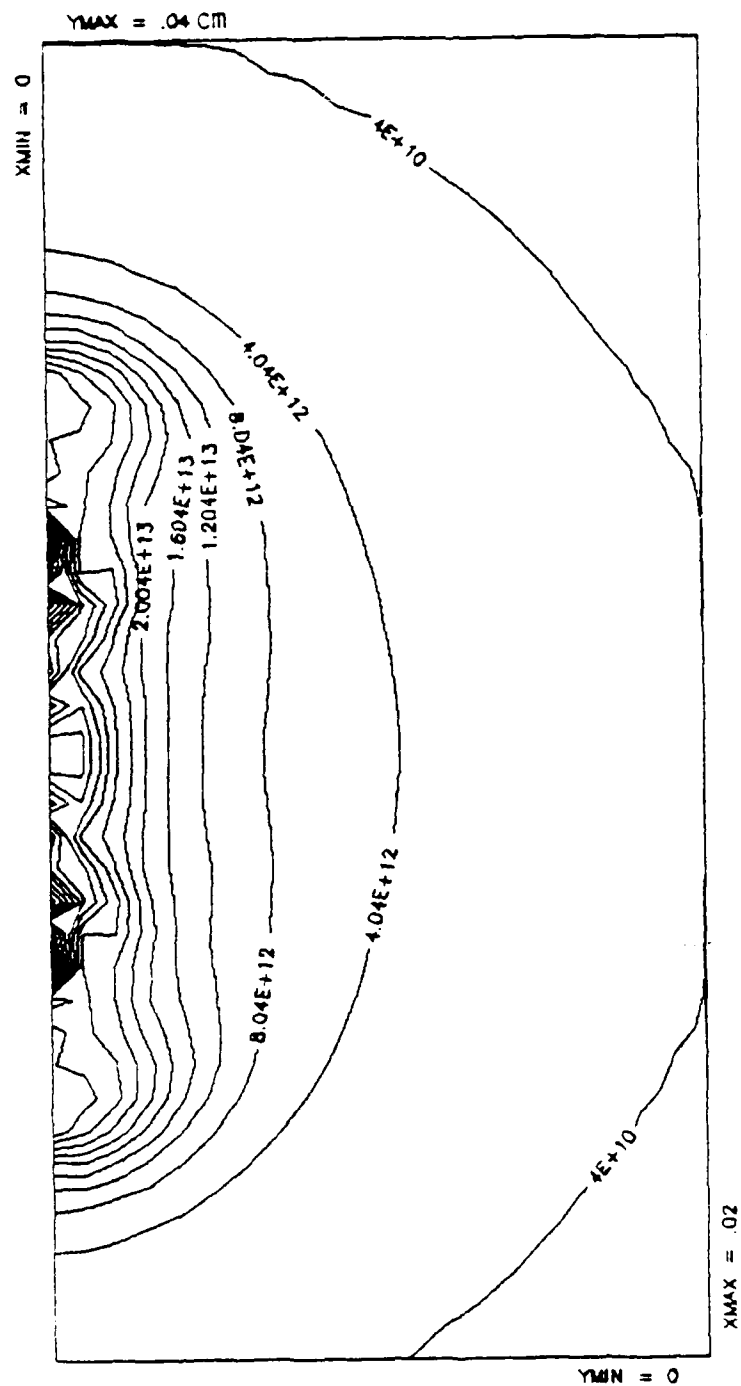


Fig. 5C. SALE Calculation for the LINUS Case at 3 nsec.



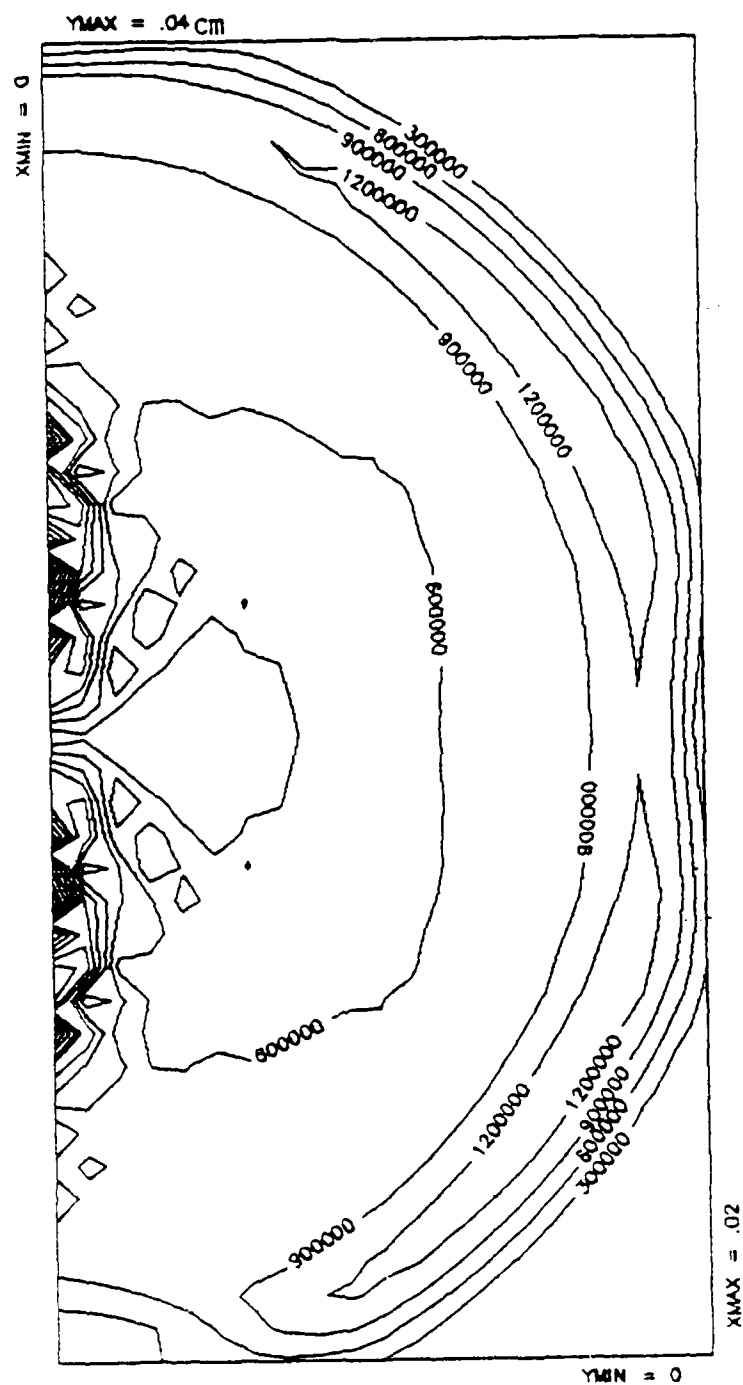
22





ENERGY(erg/g) T=5NS

Fig. 6C. SALE Calculation for the LINUS Case at 5 nsec.



SPEED(cm/sec) T=5NS

Fig. 6D. SALE Calculation for the LINUS Case at 5 nsec.

where p_s = pressure behind shock
 γ = ratio of specific heats
 ρ_0 = initial density
 r = shock front radius
 t = time.

Calculation of the shock front velocity at various times using the above equation is shown in Table 1.

TABLE 1

T(nsec)	V(shock)(SALE) 10^6 cm/sec	v(shock)(theory) 10^6 cm/sec
1	3.5	3.6
3	1.8	1.9
5	1.2	1.4

We can clearly see the excellent agreement between the shock velocity from SALE and from theory -- the difference is less than 20%. The reason for the close agreement is that modified blast wave theory does not have any loss mechanism and it assumes a constant ratio of specific heats -- assumptions which are also used in the present SALE calculation, but which will be modified for a more realistic treatment.

The calculations at 5 nsec show distinctly the reflection due to the presence of the boundary. We plan to couple the code to a regrid routine and perform a regrid with coarser grid size before the shock wave reaches the boundary in order to avoid any boundary effects. Another method would be to start with coarse grid size, but the limit on the coarsest grid size is the focal radius of the laser beam, i.e. $15 \mu\text{m}$.

From the pressure and density output, one calculates the kinetic temperature of heavy particles behind the shock front to be 10^6 K. One can also calculate this temperature using the velocity plots since velocity is proportional to the square root of the temperature. This value is an upper limit to the temperature since no radiation loss processes have yet been included.

3. Spark Dimension

In order to obtain an estimate of the time scale of emitted radiation, Sowle and Sappenfield[12] have suggested a crude calculation. This results in an estimate of the spark dimension which is very close to the actual observed spark size. The assumptions made in this calculation are: (1) all excitations result in radiative transitions, (2) no distinction is made among the different ionic states of atomic oxygen, and (3) the emitted photon energy is 10 eV. This means that the oxygen atoms are emitting radiation as hard as possible, i.e. one photon is emitted per collision.

Since the largest possible electron excitation rate coefficient expected is $\sim 10^{-8}$ cm³/sec and the assumed photon energy is 10 eV, the emission coefficient is $\sim 10^{-7}$ eV cm³/sec. Multiplying by the oxygen density of 5×10^{18} cm⁻³ (P=150 torr at room temperature) gives an energy emission rate of 1.5×10^{12} eV/sec. The SALE calculation is performed up to 5 nsec, by which time the energy expended is 8×10^3 eV.

The energy being input to the gas is 400 mJ (using the new measurement). Energy deposition calculation (see Section V.C) shows that this results in an energy input of 1.3×10^7 eV/atom. The SALE calculation for 150 torr pressure shows that the shock front radius, r , at 5 nsec is 200 μ m. We know that the energy loss, which is a measure of volumetric radiance, is directly proportional to r^3 . Therefore, if we were to increase the radius by a factor of 10, i.e. to $r=2$ mm, the energy loss would increase by a factor of 1000. At this radius, the energy loss is approximately equal to the energy input. Hence, the calculation shows that substantial energy dumping would not occur until the shock radius is 2 mm. This value is reasonably close to the observed spark size. Thus it appears from this calculation that the assumption of no energy loss at early times is valid.

D. RECOMMENDATIONS

Important information was gained in this study of the discharge region. However, this initial study has not accounted for many processes which are known to occur in the LINUS experiment, of which the main ones are the optical loss processes and the presence of plasma chemistry.

Radiation loss is a major cooling channel in an actual airburst and accounts for about 80% of the energy loss[13]. In the laser produced plasma, uv and x-ray emissions are major cooling mechanisms which are certain to reduce the temperature behind the shock front. The SALE code in its present form does not allow for any energy loss. For it to be more applicable to the analysis of the LINUS experiment, it is necessary to account for energy loss due to dissociation, excitation/ionization, and chemical reactions. In addition, we plan to include uv and x-ray deposition and pre-dosing of the gas through which the shock propagates.

Laser induced plasma contains more than one species. For the LINUS experiment we have a pool of electrons, positive atomic ions(the highest charged species identified is O^{3+}), and oxygen neutral. A tremendous amount of chemistry goes on among these species. All these chemical species should be incorporated into the code. In addition, the ideal gas equation of state does not account for intermolecular forces and is strictly only valid at low pressure and temperature. Since the LINUS plasma is high in both pressure and temperature, a more realistic equation of state should be incorporated.

Another feature which has been disregarded in the calculation is the laser pulse shape and duration. The present calculation assumes an instantaneous deposition. However, the result shows that the shock is expanding so rapidly toward the laser that the high density shock front might interact further with photons present at later time. Previously[4] the pulse shape of the laser has been measured to be spikey in normal operation with no etalon in the oscillator cavity. The pulse width given by specification is 10 nsec. Because the pulse shape is spikey, the effective pulse width is most likely less than 10 nsec. A new determination[7] gives a pulse width of 20 nsec and a smooth profile with a rise time of ~2 nsec and decay time of ~5 nsec. The new measurement is in contrast to the old one and may be due to an unaccounted time constant in the system. It is suggested that the measurement be repeated and the correct laser pulse shape be incorporated into the SALE code.

A regrid routine will be coupled to the code to calculate expansion at later times. The purpose of the regrid routine is to minimize the

number of cells in the calculation and hence shorten the runtime of the problem. Initially, one can use a small number of cells with fine grid. As the expansion develops and approaches the boundary, a regrid with coarser grid will allow the expansion to continue with no interference from the boundary.

To study whether the structures observed on the contour plots are authentic (see Figs. 4-6), one must perform sensitivity tests to see if they change as a function of grid size or number of cells or if some other parameters or effects are responsible for them.

The shape of the spark has been measured at 200 torr to show evidence for a donut around the waist of the discharge[5]. Since the focal region of the laser is bow tie shaped, the donut could arise due to interaction of shock waves moving away from the focal region (see Fig. 7). It is recommended that the rectangular focal region input to the SALE code be replaced by a "bow tie" shaped region, which is closer to reality, in order to test for effects of shock wave interaction. Should this interaction occur in the calculation, it suggests a major set of relatively inexpensive experiments for LINUS in investigations of interacting shock fronts.

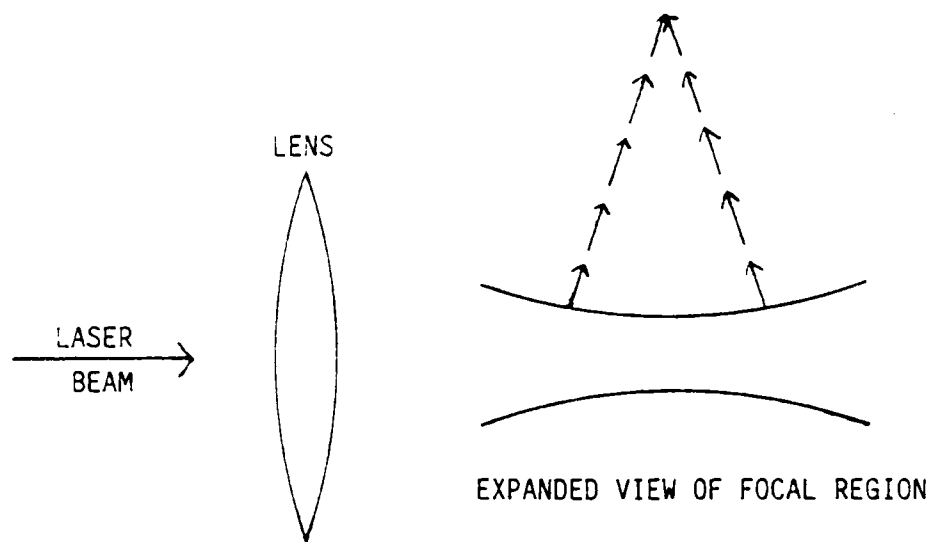


Fig. 7. Bow Tie Geometry for Laser Focal Region Illustrating Shock Wave Interaction.

III. STARK BROADENING IN HIGH ANGULAR MOMENTUM STATES OF ATOMIC OXYGEN

A. INTRODUCTION

This section describes research leading to an understanding of line broadening of high angular momentum states of atomic oxygen emitted radiation under plasma conditions. The experiments, based on the LINUS experiment, yield time resolved spectra in the infrared in the 4 μm to 10 μm spectral region. It is hoped that results will lead to measurements of electron densities of the plasma electrons, and an understanding of properties of high angular momentum states of atomic oxygen and its ions. For this study we have computed dipole matrix elements for an expanded basis set of up to 18 oxygen atom energy levels for the quintet states (6h; 6g; 6f; 5g; 5f; 4f; 7i; 7h; 7g; 7f; 5d; 4d; 8f; 8g; 8h; 8i; 8j; 6d), and have worked on an improved lineshape program.

The lineshape function is given by

$$S(\omega) = \frac{1}{\pi} \int d\epsilon W(\epsilon) R \sum_{\beta} \langle \alpha | r_{\mu} | \beta \rangle \langle \alpha' | r_{\mu} | \beta \rangle \langle \alpha | \frac{1}{[i(\omega - \omega_{\alpha\beta}) + \Phi]} | \alpha' \rangle$$

where in second order

$$\Phi_{\alpha\alpha'} = - \frac{4\pi n_e}{3} \left(\frac{e}{h} \right)^2 \sum_{\alpha''} \langle \alpha | r_{\mu} | \alpha'' \rangle \langle \alpha'' | r_{\mu} | \alpha' \rangle \int dv \frac{f(v)}{v} \int \frac{d\rho}{\rho} [A(z, z' + iB(z, z'))],$$

and where $[A(z, z' + iB(z, z'))]$ represents electron atom collision integrals, $f(v)$ the electron velocity distribution, $W(\epsilon)$ the electron microfield distribution, and other terms have their usual meanings. The term $\Phi_{\alpha\alpha'}$ represents a linewidth term.

We are working to apply this expression to the near degenerate cases of high principal quantum number and high angular momentum states. At the present time, electron collision processes are represented by a single relaxation time, T_1 and the observed linewidth is caused by this relaxation time, the spontaneous emission time, and instrument resolution. Because of the near degeneracy and the great number of J substates, and therefore the sensitivity of the system to electric field perturbations.

our spectral model consists, at this stage, of the large number of transitions possible from the perturbations of the electric microfield on these high n , high l levels.

The interaction Hamiltonian for the atom in the presence of a static field is given by

$$H = H_0 + ezE$$

where H_0 is the Hamiltonian for the free atom. The eigenvalues for these states are the known energy levels of atomic oxygen while the eigenfunctions are unknown. We have assumed hydrogenic type eigenfunctions as a first approximation. The states under consideration yield a number of transitions in the infrared from $2 \mu\text{m}$ to $16 \mu\text{m}$. Fig. 8 shows these transitions for zero plasma field and 18 basis states. Transition probabilities are obtained using appropriate hydrogenic type wave functions. In the presence of the electric microfield these basis states are connected by dipole matrix elements and the states mixed, or scrambled, becoming linear combinations of each other, $|\Psi_i\rangle = \sum_n |\phi_n\rangle \langle n|i\rangle$ where $\langle nvi\rangle$ are mixing coefficients relating the eigenfunctions of the Stark problem to the basis states. These eigenfunctions are determined by diagonalizing the Stark matrix. Because of state mixing, previously forbidden transitions are now possible. The strengths of these forbidden transitions will depend on the Stark field through the mixing coefficients. For example, the transition "6h" - "5f" is proportional to

$$|\langle \Psi_{5f} | r | \Psi_{6h} \rangle|^2 = |\sum_n \sum_k \langle 5f | n \rangle \langle \phi_n | r | \phi_k \rangle \langle k | 6h \rangle|^2$$

where the 6h, 5f refer to parent states that are now "mixed" by the plasma electric field with other states and where the matrix elements for the basis states have been calculated as a part of the Stark effect interaction. The mixing coefficients, as mentioned, are field dependent. The work done has been concerned with the calculation of these dipole matrix elements between all appropriate JM_J states, the extension of the calculation to larger basis sets, the inclusion of J substates, and finally the inclusion of M_J substates.

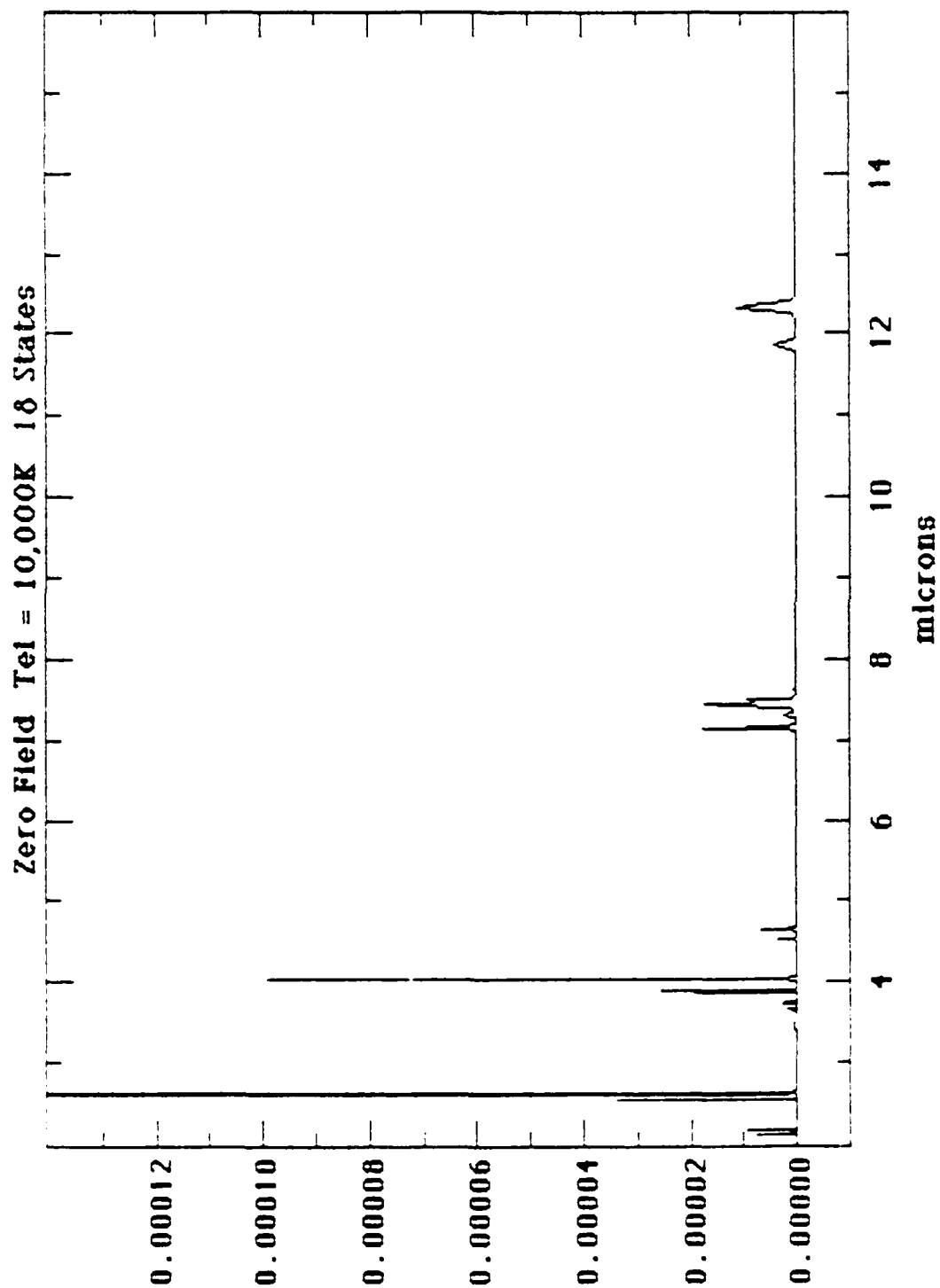


Fig. 8A. Zero Plasma Field Spectra for 18 Basis States - 2-16 microns.

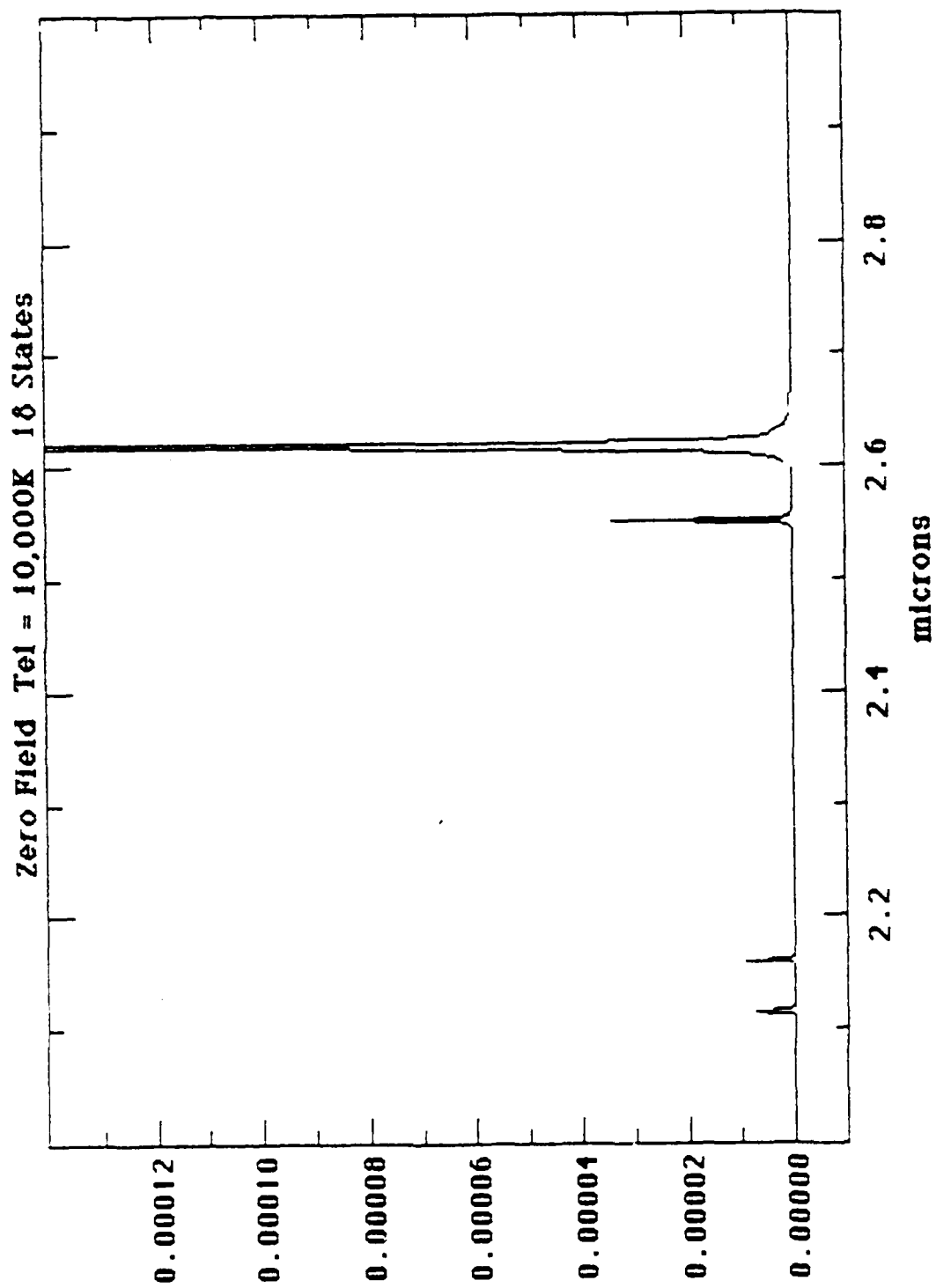


Fig. 8B. Zero Plasma Field Spectra for 18 Basis States - 2-3 microns.

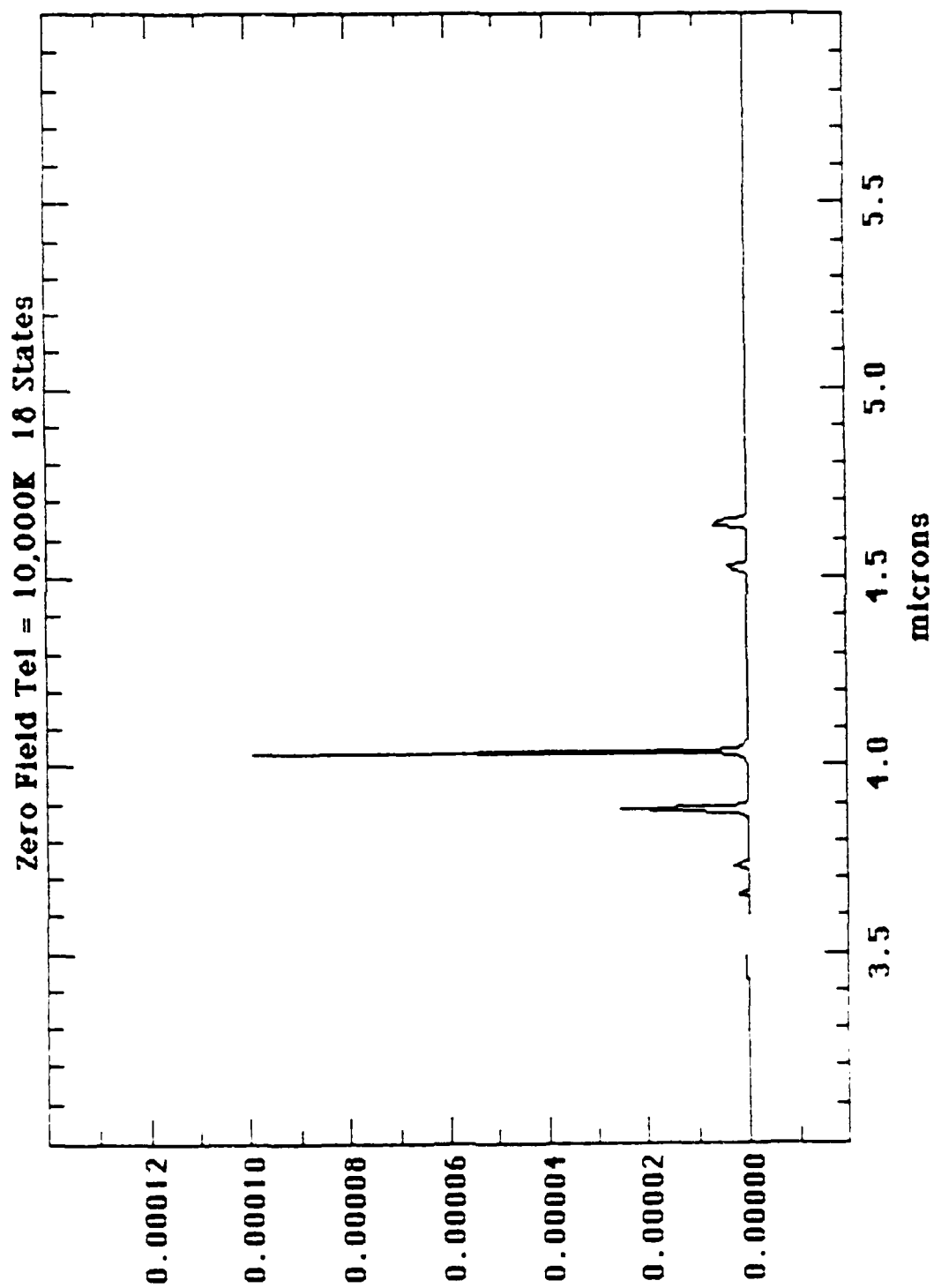


Fig. 8C. Zero Plasma Field Spectra for 18 Basis States - 3-6 microns.

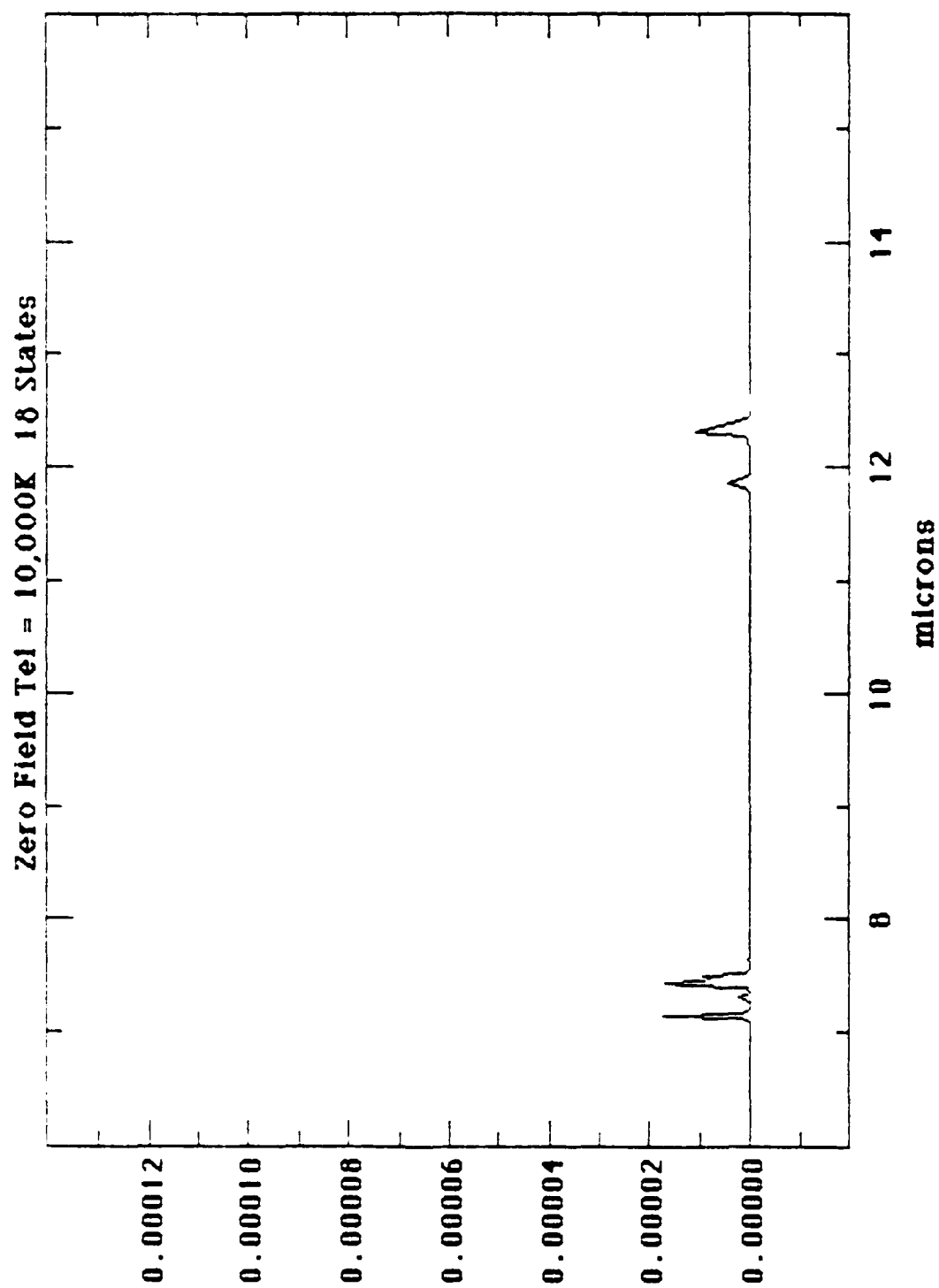


Fig. 80. Zero Plasma Field Spectra for 18 Basis States - 6-16 microns.

B. STARK CALCULATION

We have divided the Stark problem into two parts, the electron microfield that the atoms interact with, and the resulting atomic states responsible for transitions.

1. Atomic State Matrix Elements

We must calculate all matrix elements $\langle \phi_{n'J'M'L'S} | r_{\mu} | \phi_{nJMLS} \rangle$ using appropriate wavefunctions. These matrix elements will be used to construct the matrix for the Stark Hamiltonian,

$$e_0 \epsilon \langle \phi_{n'J'M'L'S} | r_{\mu} | \phi_{nJMLS} \rangle$$

and they will also be used to compute radiative transition probabilities. Diagonalization of this matrix results in eigenvalues and eigenfunctions for a given electric field. Thus, for each field we obtain eigenenergies and transition probabilities and thus a Stark spectrum. The convolution of all these thousands of lines using the fundamental widths caused by T_1 processes results in a Stark broadening line profile.

2. The Electric Microfield

In order to find the electric field, ϵ , we need to consider the problem of a fluctuating charge density (the plasma in our case). There are two traditional approximations where either the ions are stationary relative to the electron motion (high frequency approximation) or the ion motion dictates the time variation of the system (low frequency approximation). The essential physical picture is that of a sphere whose radius is given by the Debye length, $\lambda_D = (kT_e/4\pi n_e e^2)^{1/2}$, the "thickness" of the ionic atmosphere surrounding the point of interest (centered at the emitter) through which electrons travel. The electrons of density n_e have a mean radius $r_m = [3/4\pi n_e]^{1/3}$. An electron penetrating the Debye sphere at a distance r_e from the emitter provides an electric field of strength e/r_e^2 . The volume containing such charges (and hence the number distribution) depends on the radius r_e . Electrons outside the characteristic distance are exactly balanced by the background of positive charges. The actual condition is quite complicated so we shall rely on the computations of Baranger, Hooper and others for values of the field distribution. The parameter of the distribution is the ratio of the mean

electron distance to the Debye length, $\alpha = r_m/\lambda_D$ (a function of the electron number density, n_e , and the electron temperature, T_e) and the reduced electric field variable ϵ/ϵ_0 , where $\epsilon_0 = e/r_m^2$. We have chosen to fit the points calculated by Hooper to a convenient function for use in the Stark calculation. The Stark calculation begins by choosing the electron number density n_e , the electron temperature T_e , an electronic, or spectroscopic, temperature T_{el} with subsequent calculation of the microfield distribution, computation of the Stark matrix followed by matrix diagonalization. For each point on the microfield distribution there corresponds a probability of occurrence and a reduced electric field strength. The field at the emitter is the reduced field multiplied by the mean field $\epsilon_0 = e/r_m^2$. This field becomes the field part of the Stark matrix. Subsequent diagonalization gives eigenvalues, transitions and transition probabilities

$$R = W(\alpha, \epsilon/\epsilon_0) |\langle \Psi_i | r | \Psi_k \rangle|^2$$

for each point of the microfield distribution. These data are introduced into a line shape program that assumes a Lorentzian shape whose area is proportional to the transition probability weighted by an appropriate Boltzmann factor and whose width is given by relaxation processes and instrument resolution ($1/T = 1/T_1 + N_g \sigma v + \dots$).

The results for 18 states are shown in Fig. 9 for several electron densities. These are preliminary results since a number of approximations and omissions exist. First, we are considering only $S = 2$, the quintet states; second, we have not taken degeneracies into account, nor in these spectra, existence of J sublevels. Thus, the intensities are relative. Furthermore, we have parameterized electron collisions treating the problem as a static one consisting of average fields at the emitters. The essential conclusion is that the line positions are very sensitive to electron microfield strength, as expected from the near degeneracy of many of the energy levels. From a comparison of these results with the LINUS data, we conclude that the electron density is in the neighborhood of 10^{14} electrons/cm³ at a delay time of 6 μ s after initiation of the plasma.

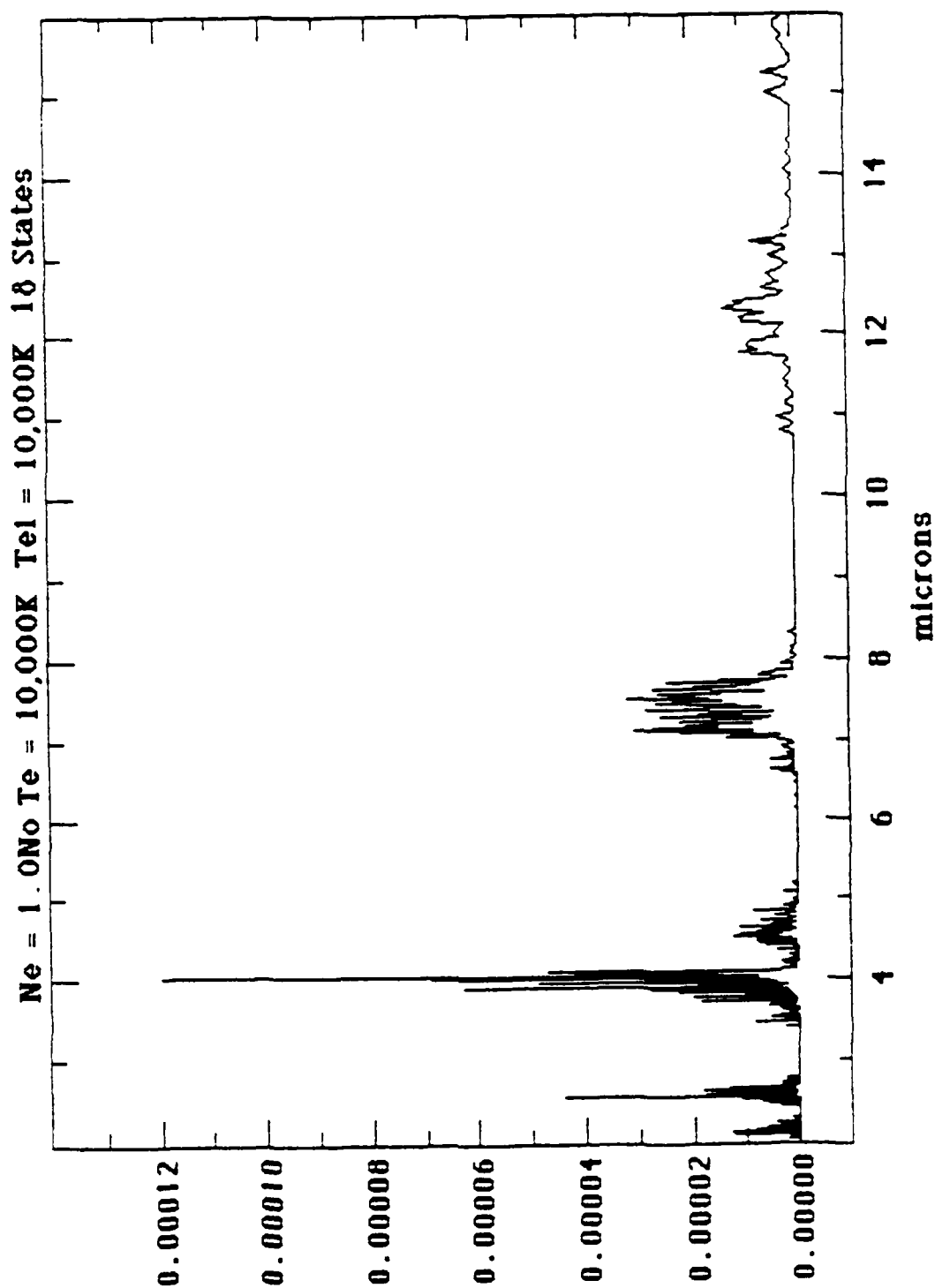


Fig. 9A. OI Spectra for 18 Basis States for Electron Densities of $10^{16}/\text{cm}^3$ - 2-16 microns.

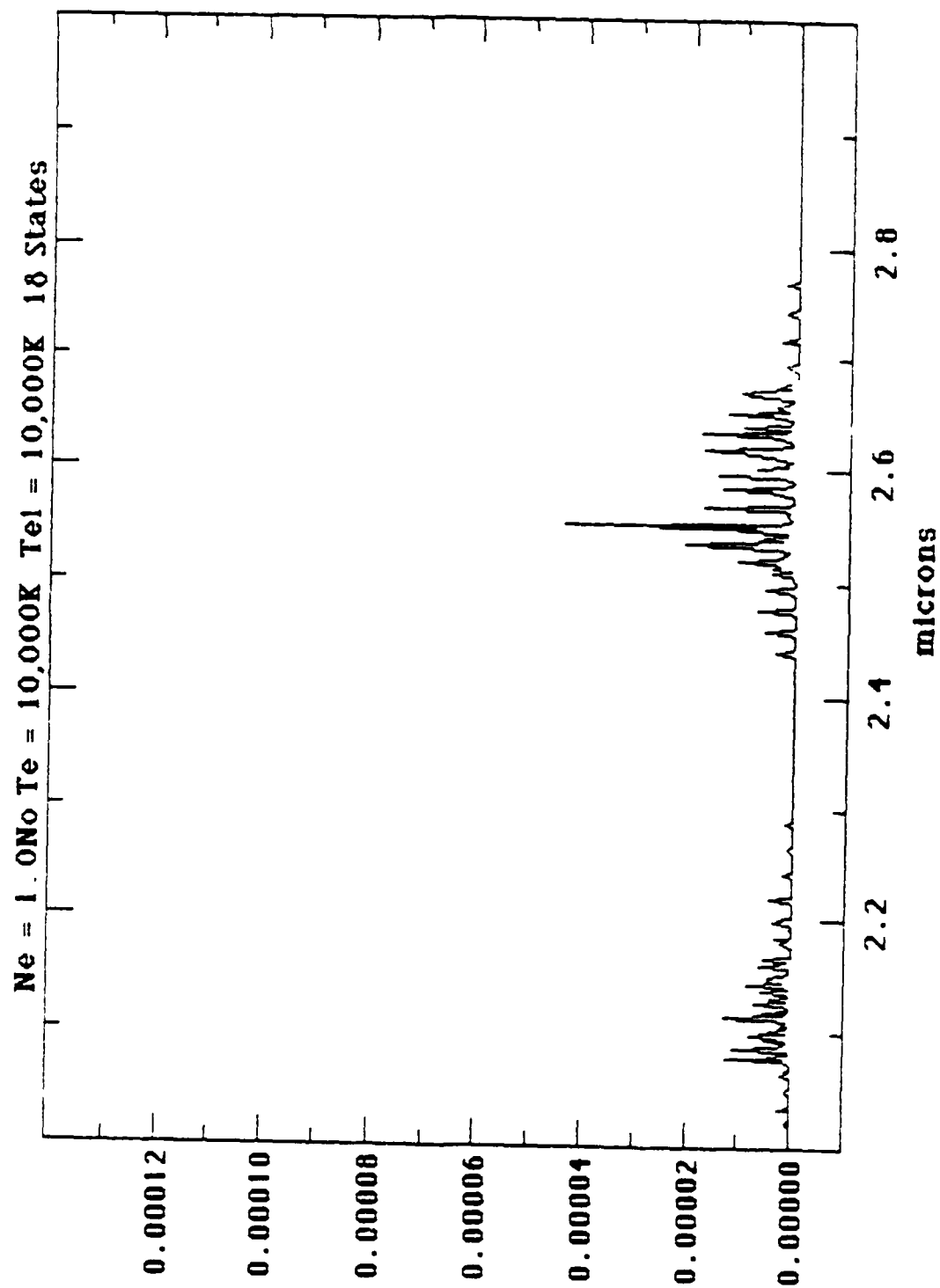


Fig. 9A.i. 0I Spectra for 18 Basis States for Electron Densities of $10^{16}/\text{cm}^3$ - 2.3 microns.

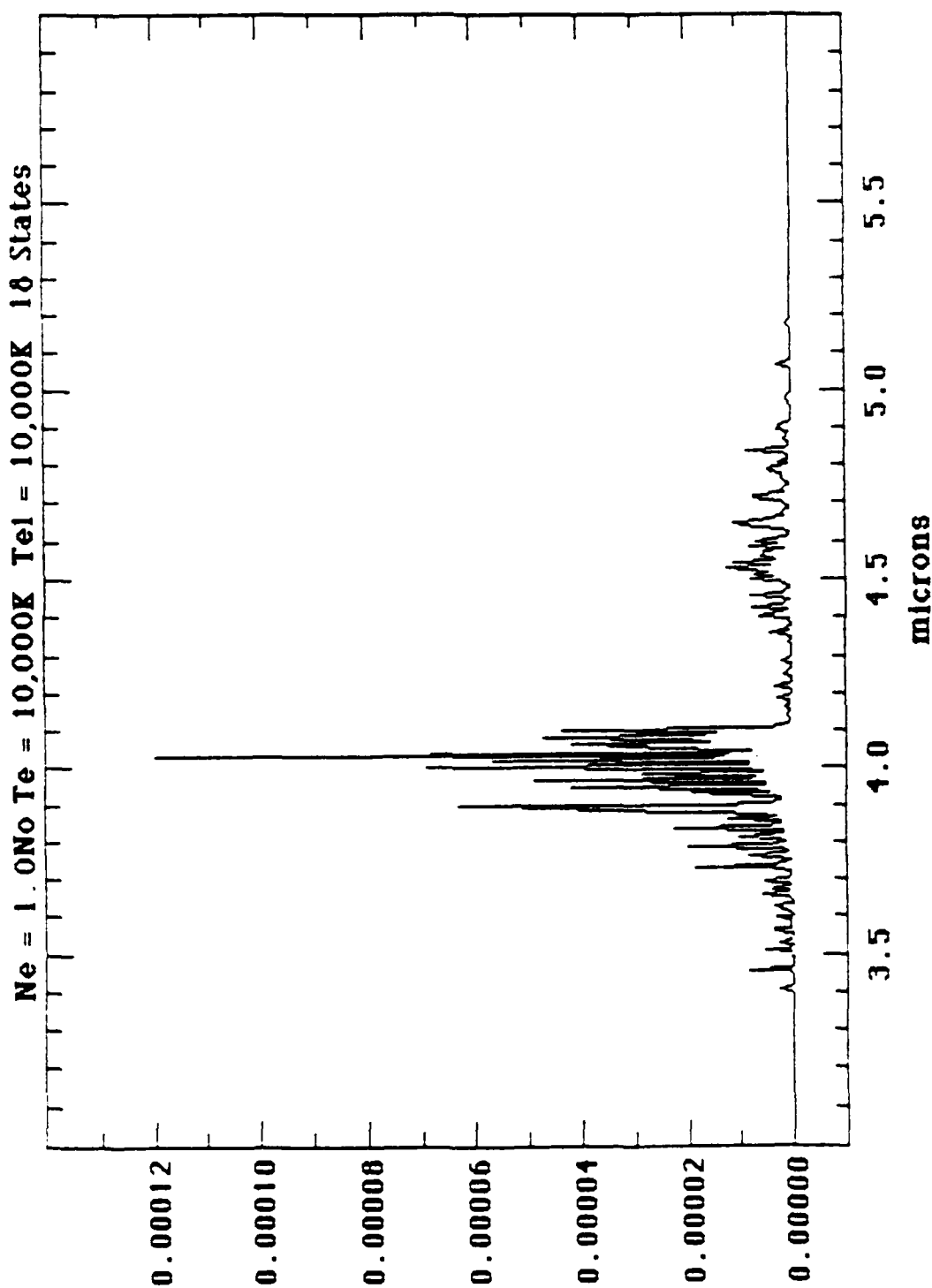


Fig. 9A. ii. 0I Spectra for 18 Basis States for Electron Densities of $10^{16}/\text{cm}^3$ - 3-6 microns.

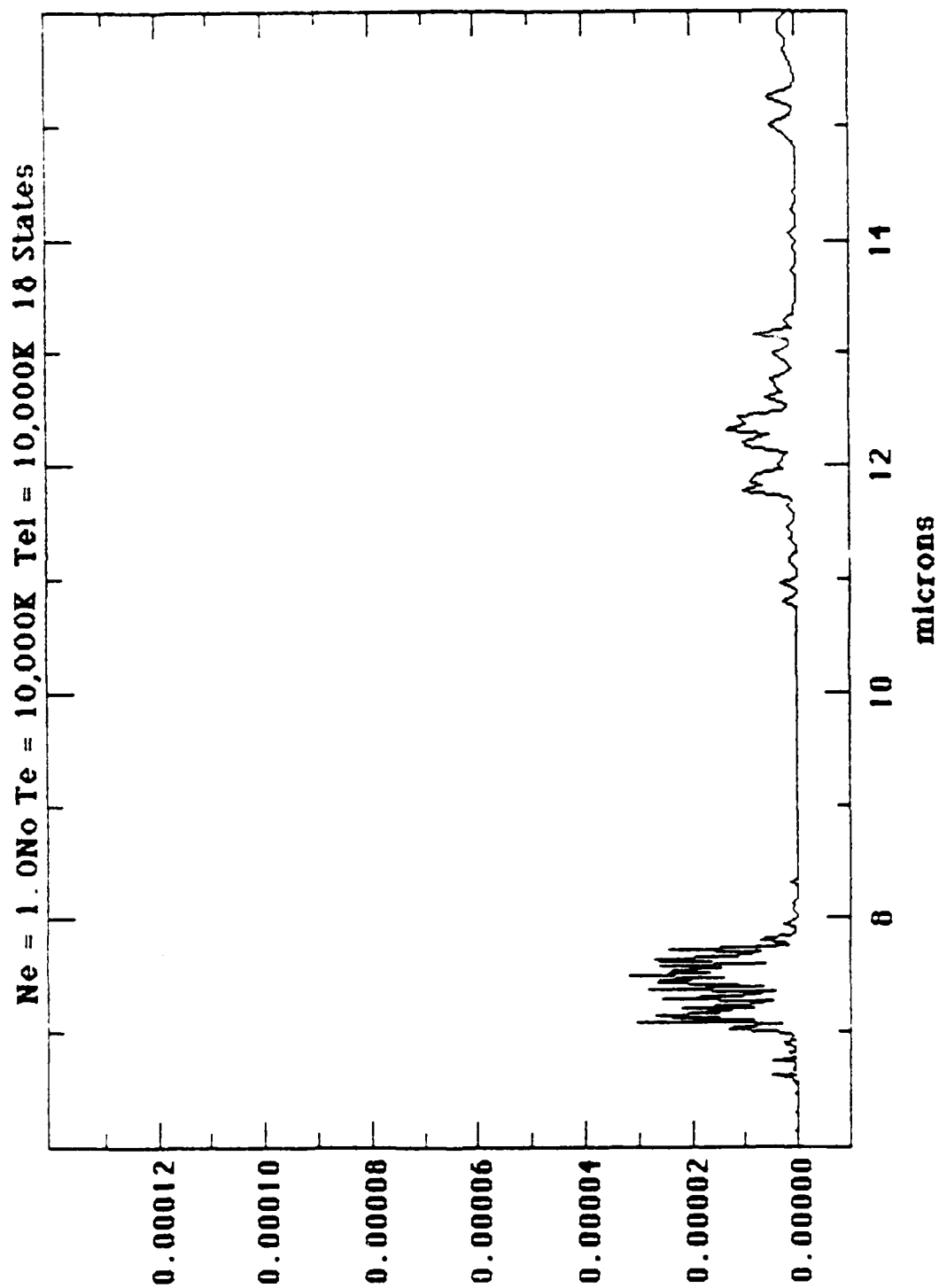


Fig. 9A.iii. 0I Spectra for 18 Basis States for Electron Densities of $10^{16}/\text{cm}^3$ - 6-16 microns.

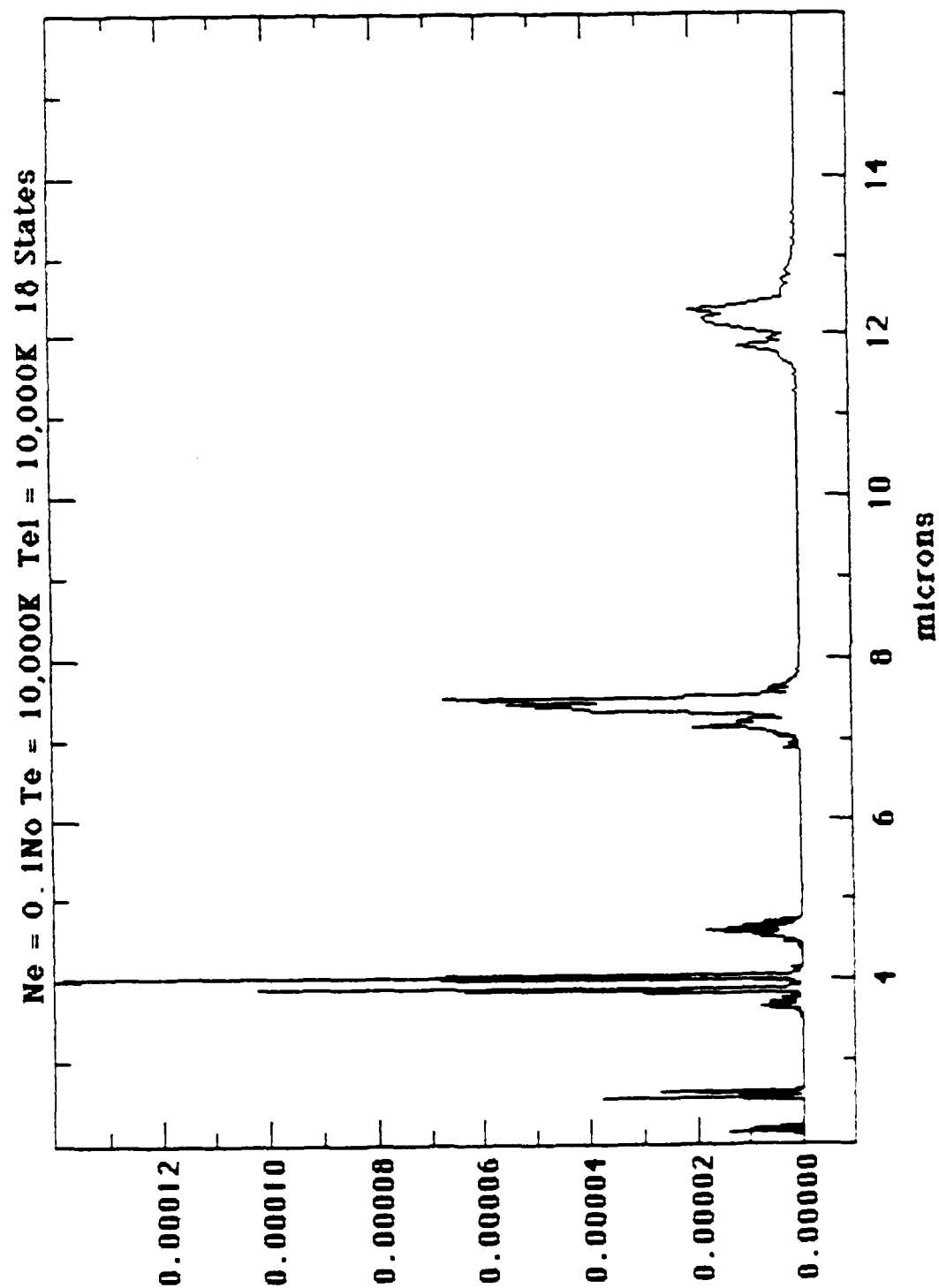


Fig. 9B. 01 Spectra for 18 Basis States for Electron Densities of $10^{15}/\text{cm}^3$ - 2-16 microns.

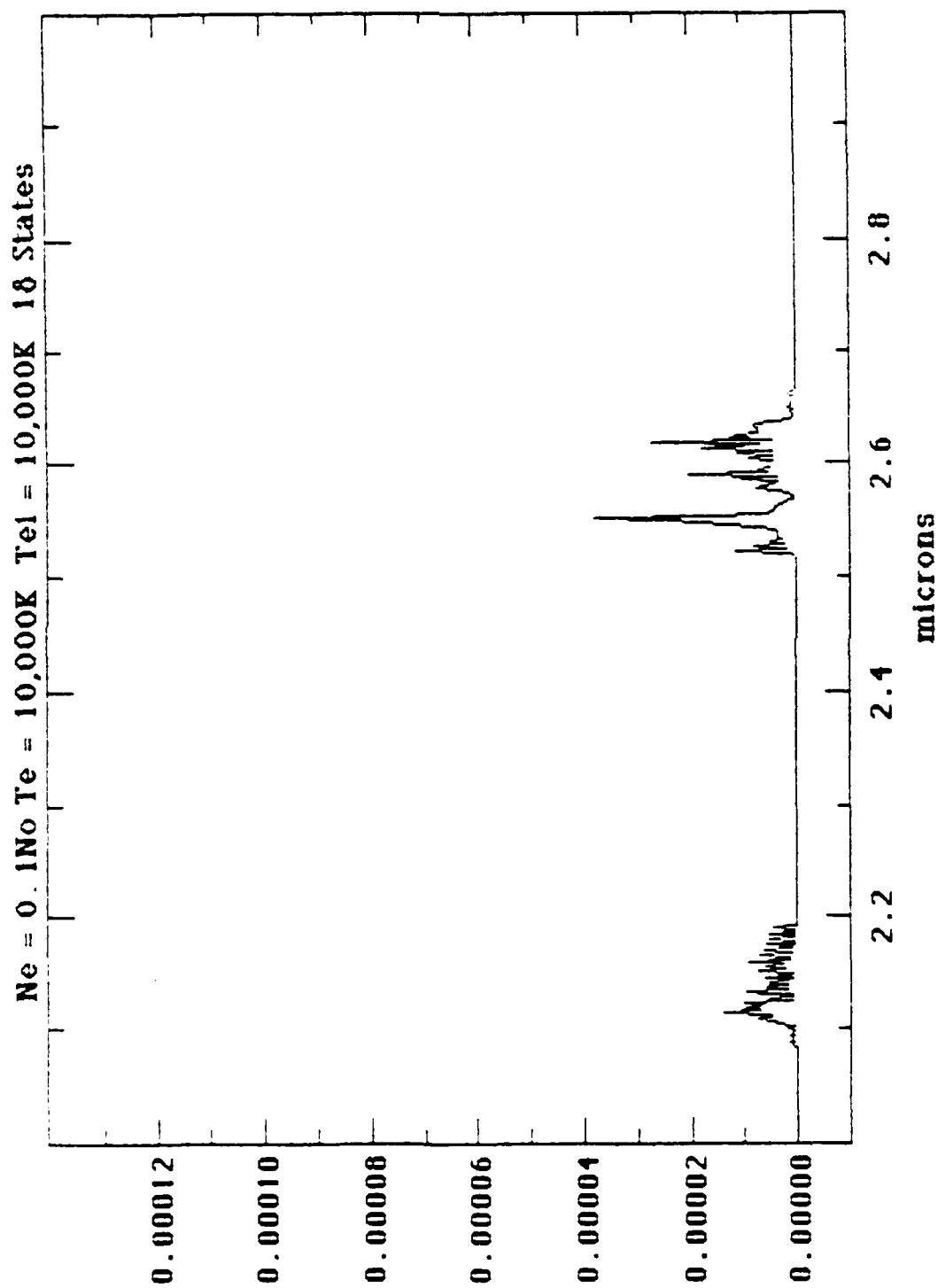


Fig. 9B.i. 01 Spectra for 18 Basis States for Electron Densities of $10^{15}/\text{cm}^3$ - 2-3 microns.

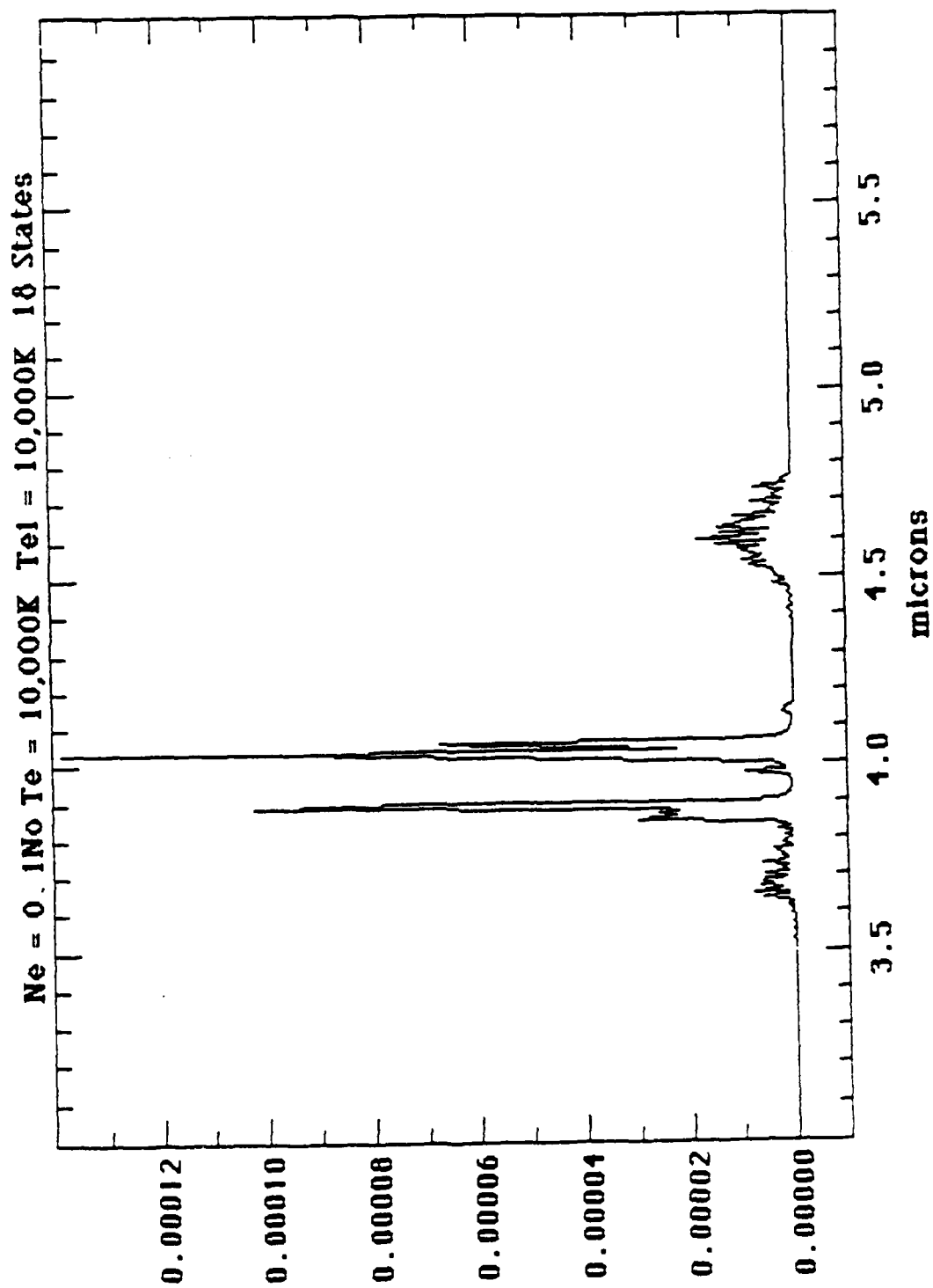


Fig. 98.ii. 0I Spectra for 18 Basis States for Electron Densities of $10^{15}/\text{cm}^3$ - 3-6 microns.

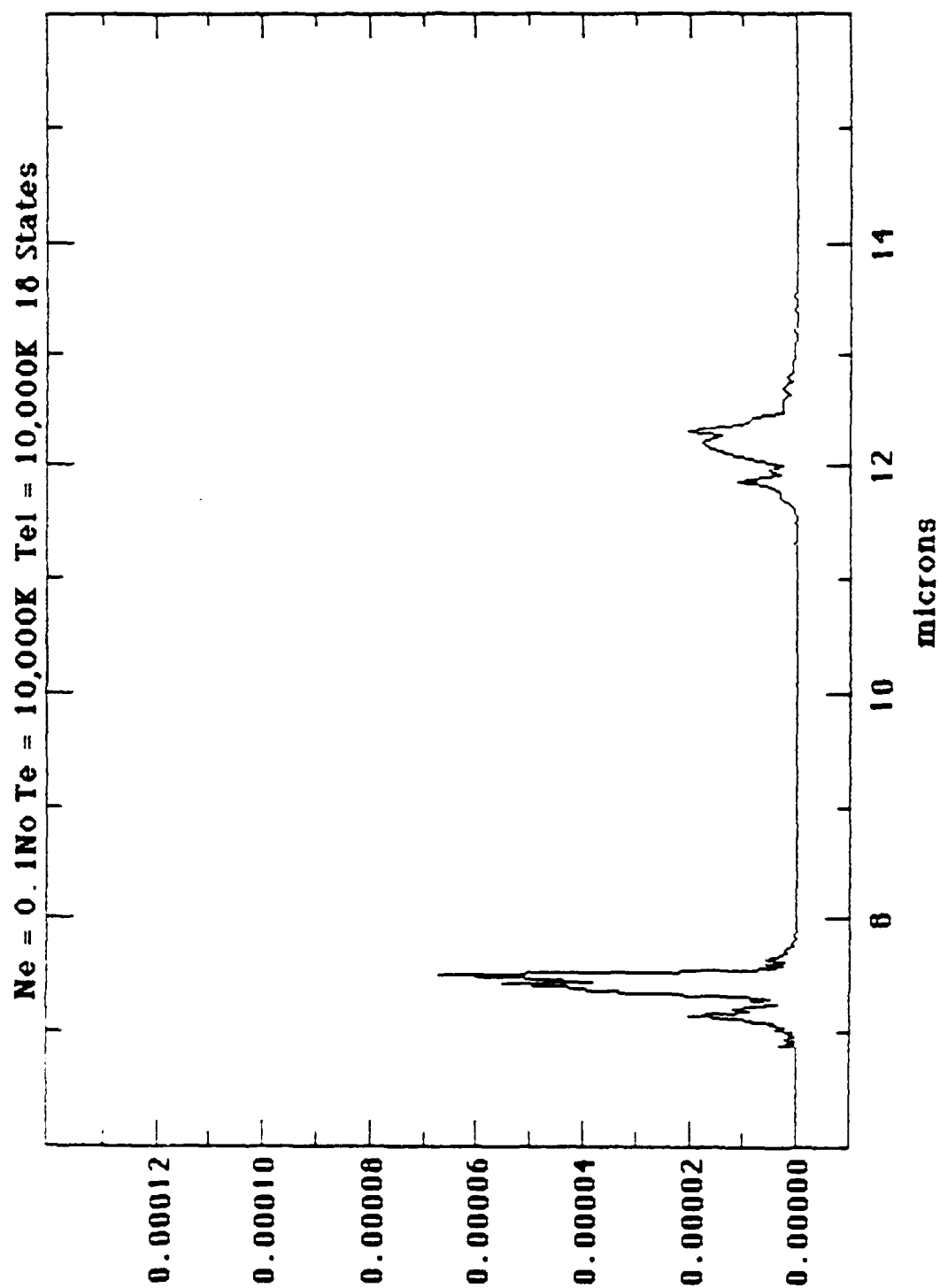


Fig. 9B.iii. 0I Spectra for 18 Basis States for Electron Densities of $10^{15}/\text{cm}^3$ - 6-16 microns.

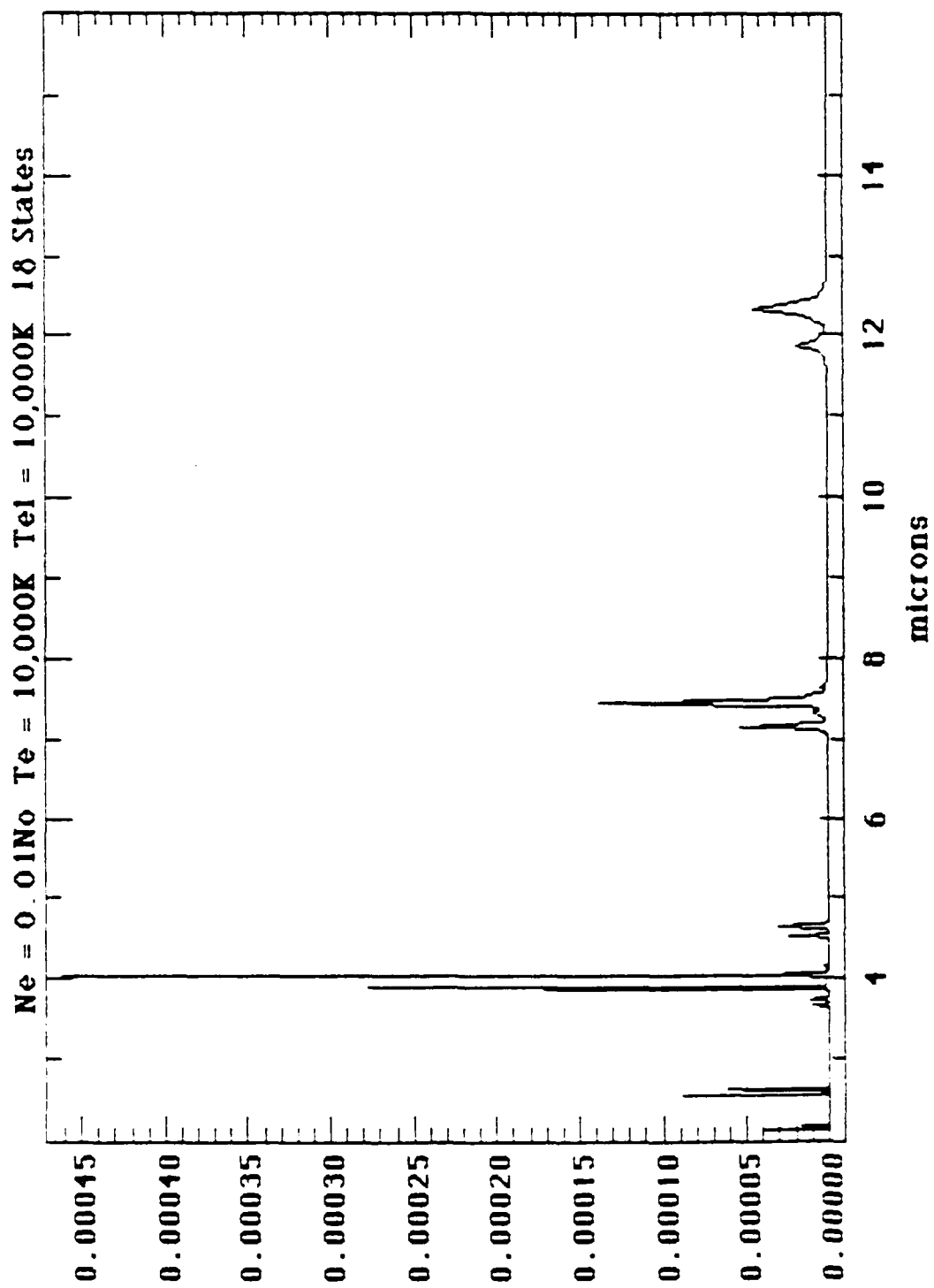


Fig. 9C. 0I Spectra for 18 Basis States for Electron Densities of $10^{14}/\text{cm}^3$ - 2-16 microns.

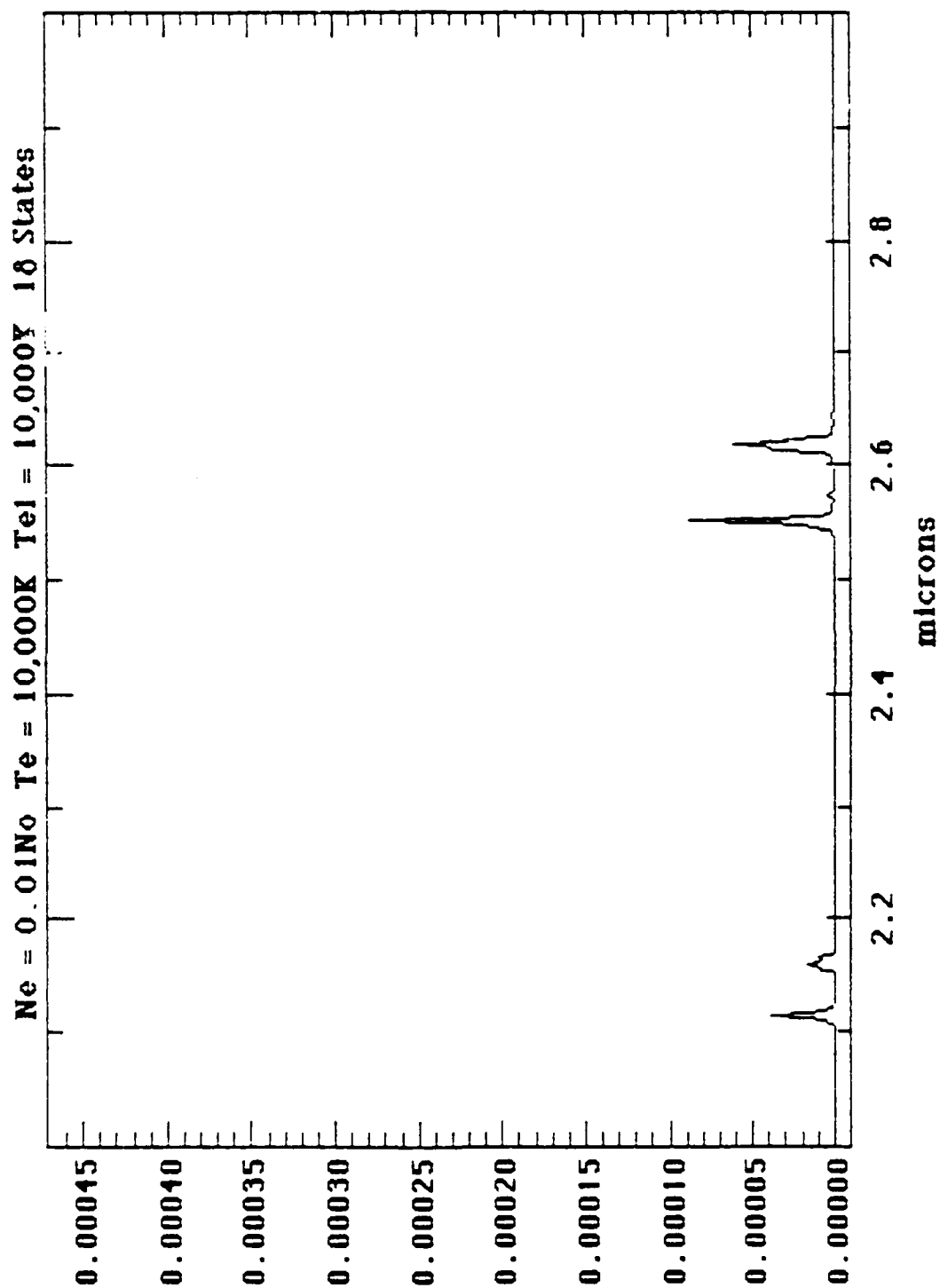


Fig. 9C.i. 0I Spectra for 18 Basis States for Electron Densities of $10^{14}/\text{cm}^3$ - 2-3 microns.

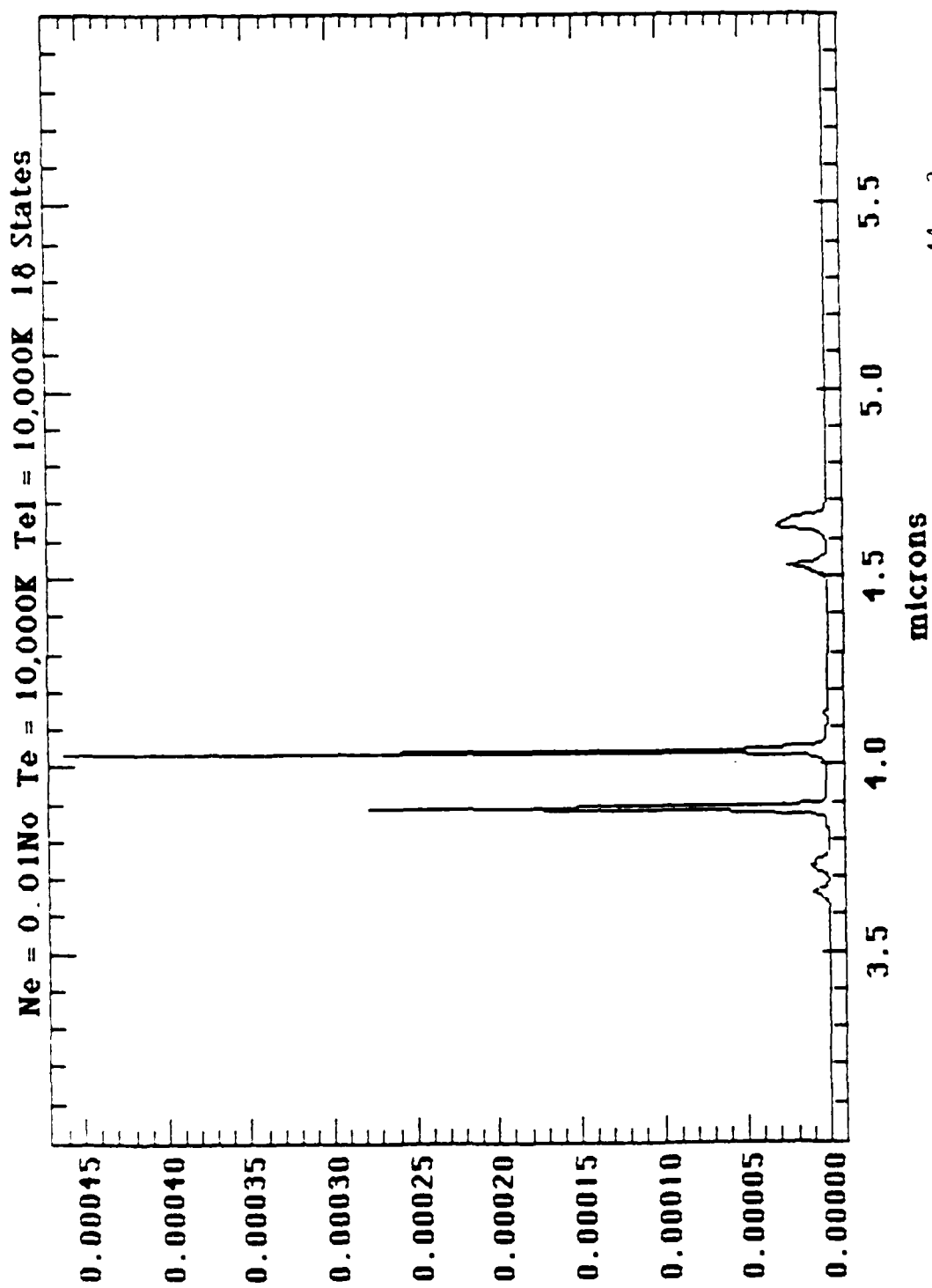


Fig. 9C. ii. 01 Spectra for 18 Basis States for Electron Densities of $10^{14}/\text{cm}^3$ - 3-6 microns.

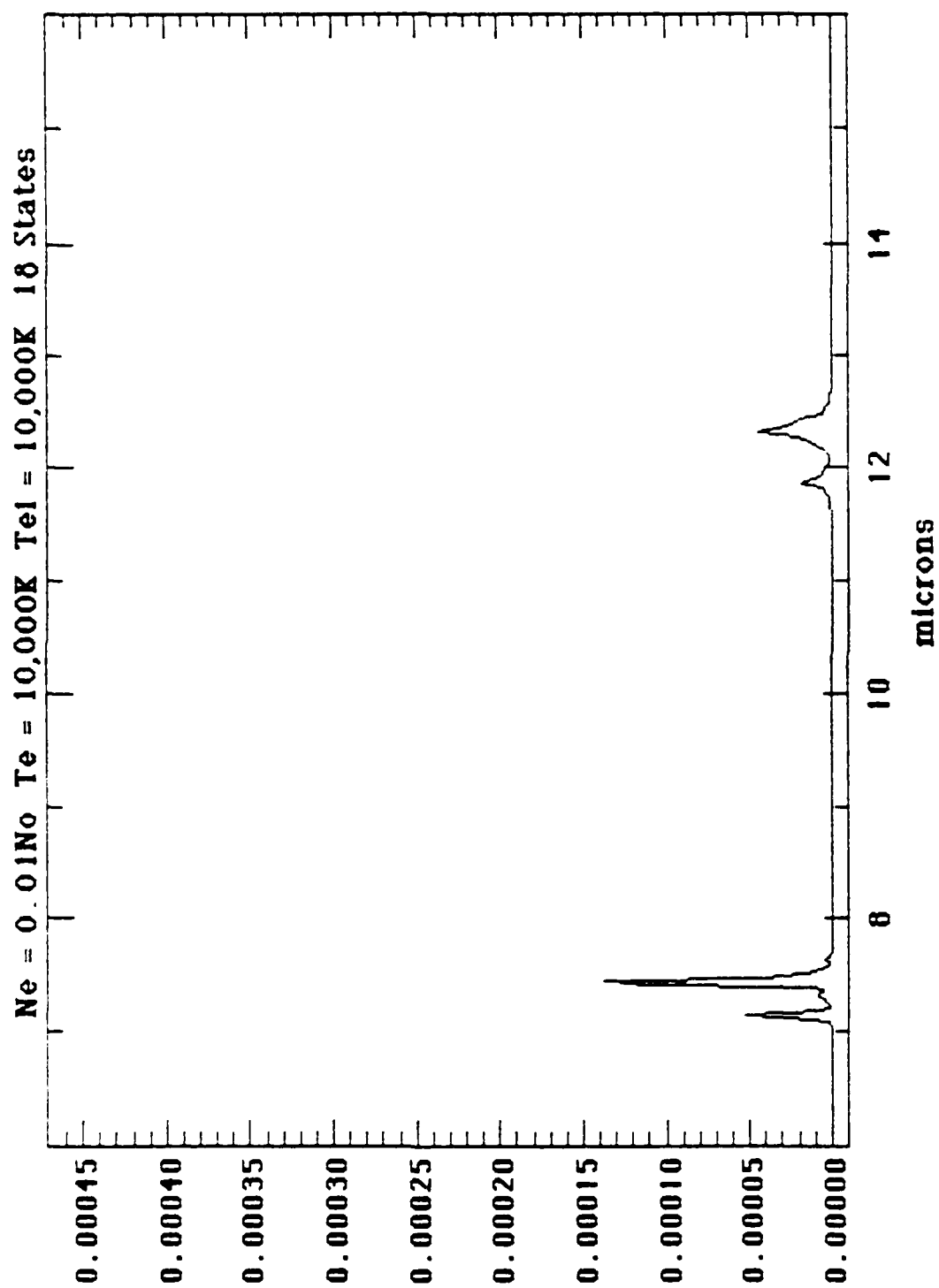


Fig. 9C.iii. 0I Spectra for 18 Basis States for Electron Densities of $10^{14}/\text{cm}^3$ - 6-16 microns.

IV. KINETIC EFFECTS

Preliminary modelling of the kinetic effects has been described in detail [4]. The initial concentrations assumed, based on energetics, are 80% O^+ , 15% O^{2+} , and 5% O^{3+} . The reaction set, which includes recombination and reionization, is shown in Table 2. The 12 kinetic equations are solved by PCCHEM, a numerical integration routine written by Gene Adams at Utah State University which has been modified by Armstrong for this calculation.

Previously[5], the time history of the species concentration was calculated by assuming an exponential temperature profile. We have now performed a new calculation using a new temperature profile obtained semi-empirically by assuming that the electrons are in collisional equilibrium with the dominant charged state. This means that the electrons are coupled with the highest charged state observed at early time (i.e. O^{3+}) and with the lowest charged state observed (i.e. O^+) at late time. The temperature profile is then determined from the latest available data on spectroscopic temperature[14] shown in Table 3. From examining this table, one observes that at early time the O^{3+} temperature is on the order of 10^5 K and decreases sharply. At 100 nsec the O^+ temperature is about 3×10^4 K and from then on varies slowly. The temperature for O neutral at late time is determined to be ~ 8000 K[15]. Thus, we assumed a temperature profile which has an exponential function from 0 to 100 nsec and behaves linearly from 100 nsec to 1 μ sec. The analytic form of the new temperature profile is

$$T = T_0[\exp(-t/2.7 \times 10^8) - 2.2 \times 10^5 t + 0.3]$$

and is shown in Fig. 10.

The results of the new calculation at 10 and 100 torr are shown in Figs. 11 and 12 respectively. The general trend of the time profile of the species concentration is the same as before. One can see that O neutral does not dominate until $t > 0.2 \mu$ sec at which time O^{3+} and O^{2+} are no longer important. Again we see the dip in O^+ at $t > 1$ nsec accompanied by an increase in O^{2+} which is attributed to reionization of O^+ .

TABLE 2

REACTION SET FOR LINUS RECOMBINATION

RXN		$k(T)=A(T/300)^b e^{-c/T}$			
1.	$0^{3+} + e + e \rightarrow 0^{2+} + e$	k_t	1.9E-18	-4.5	0
2.	$0^{3+} + e \rightarrow 0^{2+}$	k_d	6.2E-11	-1.5	5.6E3
3.	$0^{3+} + e \rightarrow 0^{2+}$	k_r	3.2E-11	-0.7	0
4.	$0^{2+} + e + e \rightarrow 0^+ + e$	k_t	5.6E-19	-4.5	0
5.	$0^{2+} + e \rightarrow 0^+$	k_d	2.8E-11	-1.5	5.6E3
6.	$0^{2+} + e \rightarrow 0^+$	k_r	1.4E-11	-0.7	0
7.	$0^+ + e + e \rightarrow 0 + e$	k_t	7.0E-20	-4.5	0
8.	$0^+ + e \rightarrow 0$	k_d	6.9E-12	-1.5	5.6E3
9.	$0^+ + e \rightarrow 0$	k_r	3.5E-12	-0.7	0
10.	$0 + e \rightarrow 0^+ + e + e$	k_i	1.7E-12	1.5	1.6E5
11.	$0^+ + e \rightarrow 0^{2+} + e + e$	k_i	6.4E-13	1.5	4.0E5
12.	$0^{2+} + e \rightarrow 0^{3+} + e + e$	k_i	4.1E-13	1.5	6.4E5

$$T = T_0 [\exp(-t/2.17E-8) - 2.2E5t + 0.3]$$

k_t =three-body, k_d =dielectronic, k_r =radiative, k_i =re-ionization

TABLE 3

O^{n+} SPECTROSCOPIC TEMPERATURES (10^4) DERIVED FROM
BOLTZMANN ANALYSIS OF LINUS SPECTRAL LINES BETWEEN 3000Å AND 8000Å

TIME (NS)	P = 10 TORR		P = 19 TORR		P = 55 TORR		P = 111 TORR		P = 173 TORR	
	O^+	O^{+2}	O^+	O^{+2}	O^+	O^{+2}	O^+	O^{+2}	O^+	O^{+2}
25	ND	ND	2.7	5.0	3.0	11	12	3.3	14	15
50	2.9	5.3	2.7	5.3	3.3	8.9	13	3.2	12	15
100	3.3	5.5	2.8	4.8	3.1	6.7	12	3.1	11	16
150	3.0	5.0	2.9	4.9	3.0	6.5	12	2.6	9.5	14.5
180	ND	ND	2.7	4.8	2.4	6.7	9.0	2.6	8.8	10.5
200	ND	ND	2.3	5.5	2.5	6.5	9.0	2.2	8.0	8.5
250	3.3	5.0	2.2	5.1	2.5	5.5	6.9	2.6	7.2	7.5
300	ND	ND	3.0	5.0	2.6	4.8	NS	2.3	6.1	7.6
400	ND	ND	2.8	4.8	2.4	5.0	NS	2.3	6.1	6.0
650	ND	ND	2.8	4.9	2.5	5.0	NS	2.5	4.2	6.0
900	ND	ND	3.3	4.1	2.8	4.3	NS	2.4	5.0	NS

NS - NO SIGNAL

ND - NO DATA

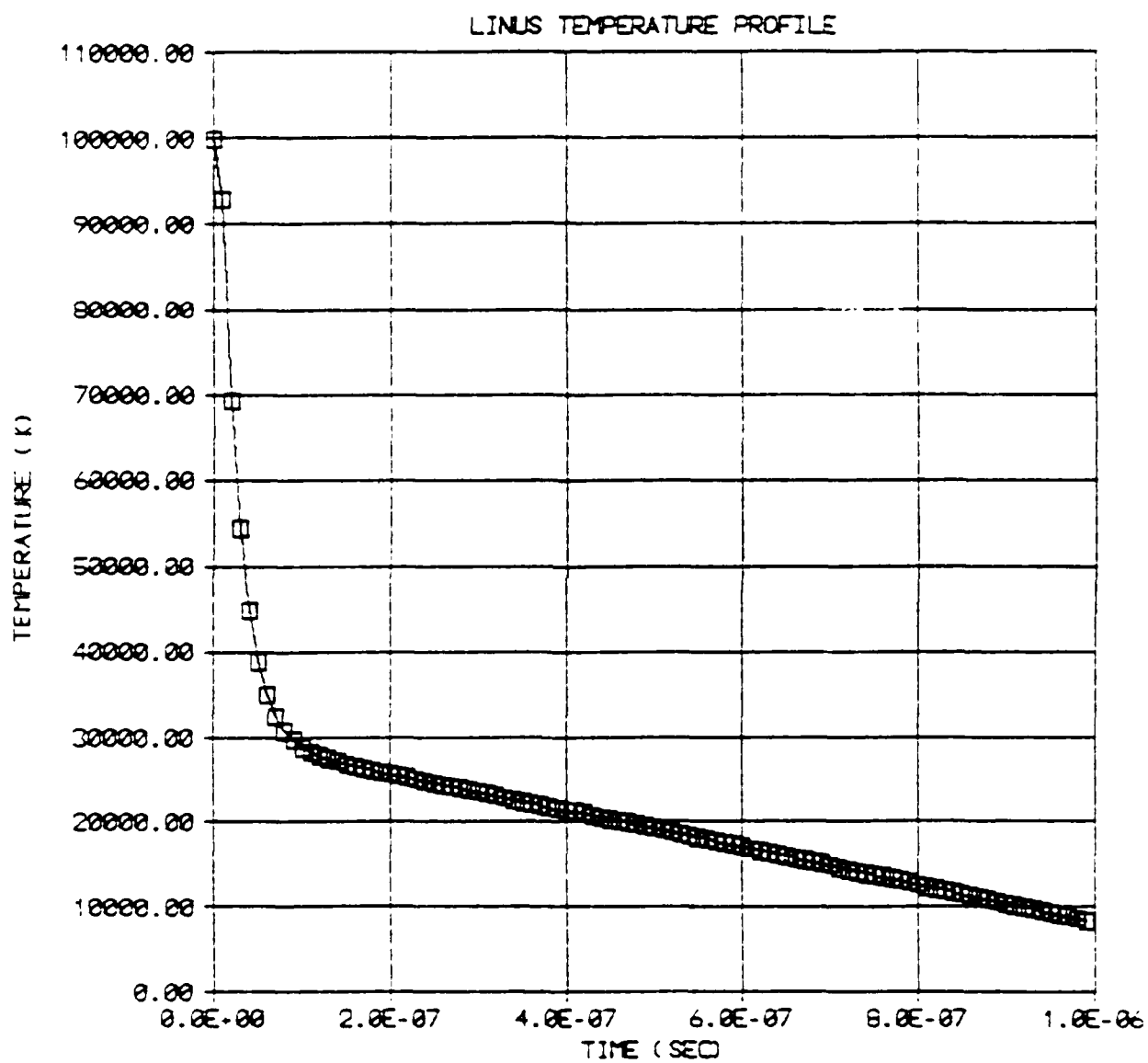


Fig. 10. Assumed Temperature Profile for Kinetic Calculation.

$$T = T_0 [\exp(-t/2.17E-8) - 2.2E5 t + 0.3]$$

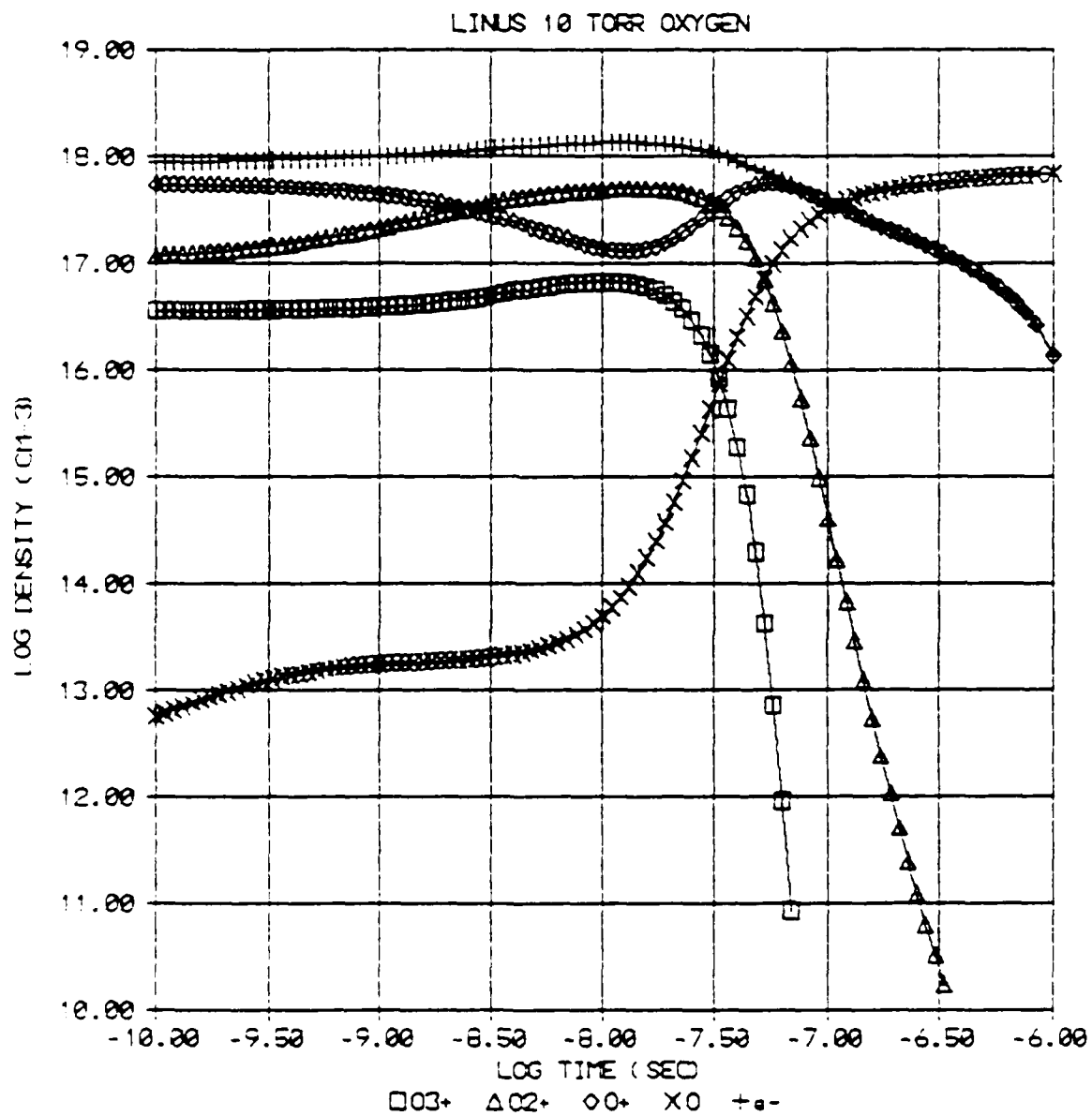


Fig. 11. Calculated log density of species as a function of time for 10 torr oxygen.

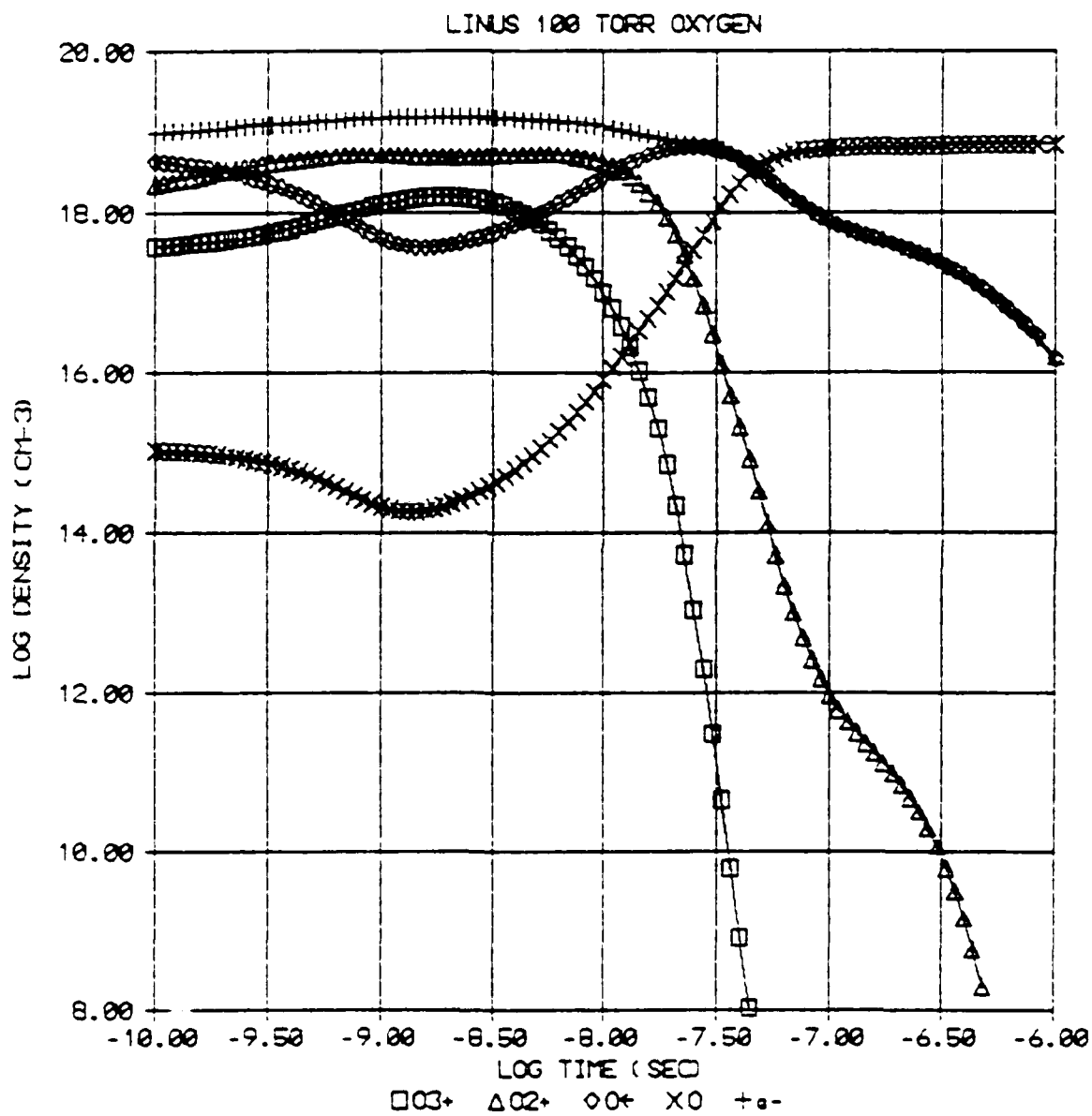


Fig. 12. Calculated log density of species as a function of time for 100 torr oxygen.

Because the new profile has lower temperatures throughout most of the time domain, two differences in the new calculation are observed. First, we see a general trend of compression for all species at early time. Second, the electron and O^+ densities are higher by a factor of 5 at 1 μ sec in the new result. The two differences can be explained by the fact that the dominant three-body recombination rate is an inverse function of temperature. The recombination rate using the new profile is higher and hence accelerates the early time build up of lower charged species. Similarly, the temperature of the new calculation at 1 lsec is higher (8000 K vs. 4000 K). Hence, the slower recombination rate results in a higher electron and O^+ densities at late time.

The assumptions used in this calculation may be incorrect but they give us a good place to begin the model and will help us in pursuing further more detailed modelling which will include time dependent terms for all the excited states in each species.

V. MISCELLANEOUS ISSUES

A. Spherical Aberrations

The purpose of this calculation is to determine whether the lens used in the LINUS experiment is a source of spherical aberration.

The number of wavelengths of spherical aberration is given by[16]

$$m = \frac{\Phi(p)}{\lambda} = \frac{-(ap)^4}{8\lambda f^3} \left[\frac{n^2}{4(n-1)^2} - \frac{n}{4(n+2)} + \frac{(n+1)^2}{n(n+2)} \right]$$

where m = aberration number(wavelengths)

$p = r/a$ = radial distance(cm) from optical axis at front lens
surface divided by lens radius(cm)

λ = wavelength(cm)

n = index of refraction of lens material

f = lens focal length(cm).

For $n = 1.55$, this reduces to

$$m = \Phi(r)/\lambda = -3.056r^4/8\lambda f^3.$$

For r_{\max} = beam radius = 0.3 cm,

$$m = -0.166 \text{ wavelengths (minus sign means towards the beam source).}$$

This result is consistent with figure 9.2, p. 722 from Morgan's article[16] which shows that for a 6 mm beam at 1.06 μm wavelength, $\Phi < 0.2$ at a 5.6 cm focal length. For a 4.1 cm focal length lens, $m = -0.42$ wavelengths. Thus the calculation shows that spherical aberration caused by the present lens is negligible.

B. Focal Volume Description

The radius of the focal volume is given by the thin lens approximation from geometrical optics[17]. The thin lens approximation is valid if the lens thickness is small with respect to the focal length. For the LINUS lens, this ratio is < 0.1 so the thin lens approximation is probably valid. In this case one obtains for the beam diameter

$$\tan\theta/2 = (d/2)/f$$

where f = lens focal length

$\theta/2$ = half-angle laser beam divergence(radians)

$d/2$ = half-diameter focal waist

which, for small angles reduces to

$$d/2 = r = f(\theta/2)$$

For LINUS, $\theta/2 \approx 0.25$ milliradians, and $f = 5.8$ cm, thus $r \approx 15 \mu\text{m}$.

For the focal length, l , the general definition is given as that distance where the intensity drops to half of that at the focal plane. Again, from the thin lens approximation and geometrical optics arguments[16],

$$l = 2(\sqrt{2} - 1)f^2\theta/D$$

where the variables are defined above and

D = unfocussed beam diameter at the lens surface.

For our case, $D \approx 6.5$ mm, thus $l \approx 110 \mu\text{m}$.

For the new focal length measurement, $f = 4.1$ cm, $r = 10 \mu\text{m}$ and $l = 54 \mu\text{m}$.

These numbers are valid to the extent that the thin lens approximation is appropriate and to the extent that self-focussing is unimportant. However, any uncertainties in these numbers are likely to be much less than uncertainties in other areas that are more critical to our analysis.

C. Energy Deposited per Molecule

Given an initial laser power, it is instructive to calculate the maximum amount of energy which could be deposited onto each O_2 molecule. The number of molecules in the laser focal volume, n , is given by

$$n = NV,$$

where N = number density of molecules, and

V = focal volume of laser.

For a pressure of 150 torr at room temperature, $N = 4.8 \times 10^{18} \text{ cm}^{-3}$. The focal volume, V , is

$$V = \pi r^2 l.$$

where r = focal radius, and

l = length of the focal region.

The two parameters, r and l , can be calculated using the focusing lens formula (see Section V.B). For the lens used in the experiment (focal length of 4.1 cm), $r=10 \mu\text{m}$ and $l=54 \mu\text{m}$. This results in a focal volume of $2 \times 10^{-8} \text{ cm}^3$. Hence, the number of O_2 molecules in the focal volume is $\sim 10^{11}$. The initial laser energy is $\sim 1 \text{ J}$ per pulse and typically 40% of this energy is absorbed[7]. Therefore, the maximum energy deposited is $\sim 10^7 \text{ eV}$ per O_2 molecule.

The dissociation energy is 5.2 eV. The first, second, and third ionization potential of O atom are respectively 13.6, 35.2, and 55.0 eV. Thus the generation of two O^{3+} ions from one O_2 molecule requires energy of 213 eV. This quantity is a minute fraction of the initial laser energy. This implies that most of the energy is going into PV (pressure volume) work.

D. Momentum Transfer

Another issue which needs to be addressed is the shift of the spark location as a result of momentum transferred from the high power laser beam to the gas. The momentum of a photon, M , is given by

$$M = 2E/v,$$

where $E=h\nu$ is the photon energy and $v=c$ is the velocity of light. For photon of wavelength $1.06 \mu\text{m}$, $M=1.3 \times 10^{-22} \text{ g-cm/sec}$.

The distance shifted due to photon momentum imparted to the molecules, Δx , is

$$\Delta x = M \Delta t / m,$$

where Δt =effective pulse width is assumed to be 2 nsec and m =mass of O_2 molecules in the focal volume ($P=150 \text{ torr}$ and $T=298 \text{ K}$) is $5 \times 10^{-12} \text{ g}$.

Therefore, Δx is 5.2×10^{-20} cm per photon. Since the amount of energy contained in a $1.06 \mu\text{m}$ photon is 2×10^{-12} erg, the initial laser energy of 400 mJ is equivalent to 2×10^{18} photons per pulse. The final distance shifted due to momentum transfer should be 1 mm; however, no such shift has been detected by eye. In fact, the shift may be offset by laser-shock front interactions which cause the spark to elongate toward the laser. Thus this issue is yet not fully resolved.

E. Continuum

If data on early time continuum can be described by bremsstrahlung in the field of an ion, then values for electron density and temperature can be obtained. The spectral emission coefficient for free-free transitions in the field of an ion, ϵ_ν , is given by[11]

$$\epsilon_\nu = \frac{32\pi}{3} \left(\frac{2\pi}{3mkT} \right)^{1/2} \frac{e^6}{mc^3} N_e \exp(-h\nu/kT) \sum_i Z_i^2 N_i^+$$

where m = electron mass

k = Boltzmann's constant

T = electron gas temperature

e = electron charge

c = velocity of light

N_e = electron density

h = Planck's constant

ν = frequency of transition

Z_i = charge of i th ion

N_i^+ = density of i th ion.

Since the highest charged state observed in the line spectra is O^{3+} , we assume that early time continuum is also dominated by O^{3+} . With this assumption, the summation in the above is reduced to one term: $Z_i=3$ and $N_i^+=(1/3)N_e$. The equation is then simplified to

$$\epsilon_\nu = \text{constant} \times N_e^2 T^{-1/2} \exp(-h\nu/kT)$$

Fig. 13 is a plot of the emission coefficient on a relative scale as a function of wavelength. The spectral region covered is 3000 to 5000 Å with the electron density being 10^{14} cm^{-3} . We can see from the figure that the functional form of the emission coefficient changes for different values of the electron temperature. Therefore, by obtaining emission coefficients from experimental continuum spectra, we can compare the functional form of the experimental coefficients to sets of curves of calculated coefficients for different temperatures. The calculated curve which most closely matches the observed form will give value for the electron temperature.

For a fixed temperature the effect of varying the electron density is to change the absolute scale of the emission coefficient with the functional form remaining unchanged. Thus to obtain electron density one would need an absolute calibration of the experimental emission coefficient.

F. CVF vs. SPEX

The purpose of this calculation is to determine whether there is any real advantage in using the OCLI CVF over the SPEX 1870 spectrometer in the LINUS experiment. Two approaches are used: one calculates the net radiance reaching the detector and the other calculates the net throughput.

1. Net radiance

a. Spectrometer

The SPEX 1870 is a 0.5 m monochromator which consists of two mirrors and a grating in a Czerny-Turner configuration. Its $f/\#$ is 6.9 and is related to the solid acceptance angle, Ω , by

$$\Omega = \pi/(4f/\#^2) = 0.017 \text{ sterad.}$$

The slit width used in the LINUS experiment is 3 mm and this corresponds to nominal resolutions of $0.02 \text{ } \mu\text{m}$ in the SWIR and $0.04 \text{ } \mu\text{m}$ in the MWIR and LWIR.

If we start with a point source of radiance, N_p , and using a lens which matches the $f/\#$ of the spectrometer, the radiance entering the

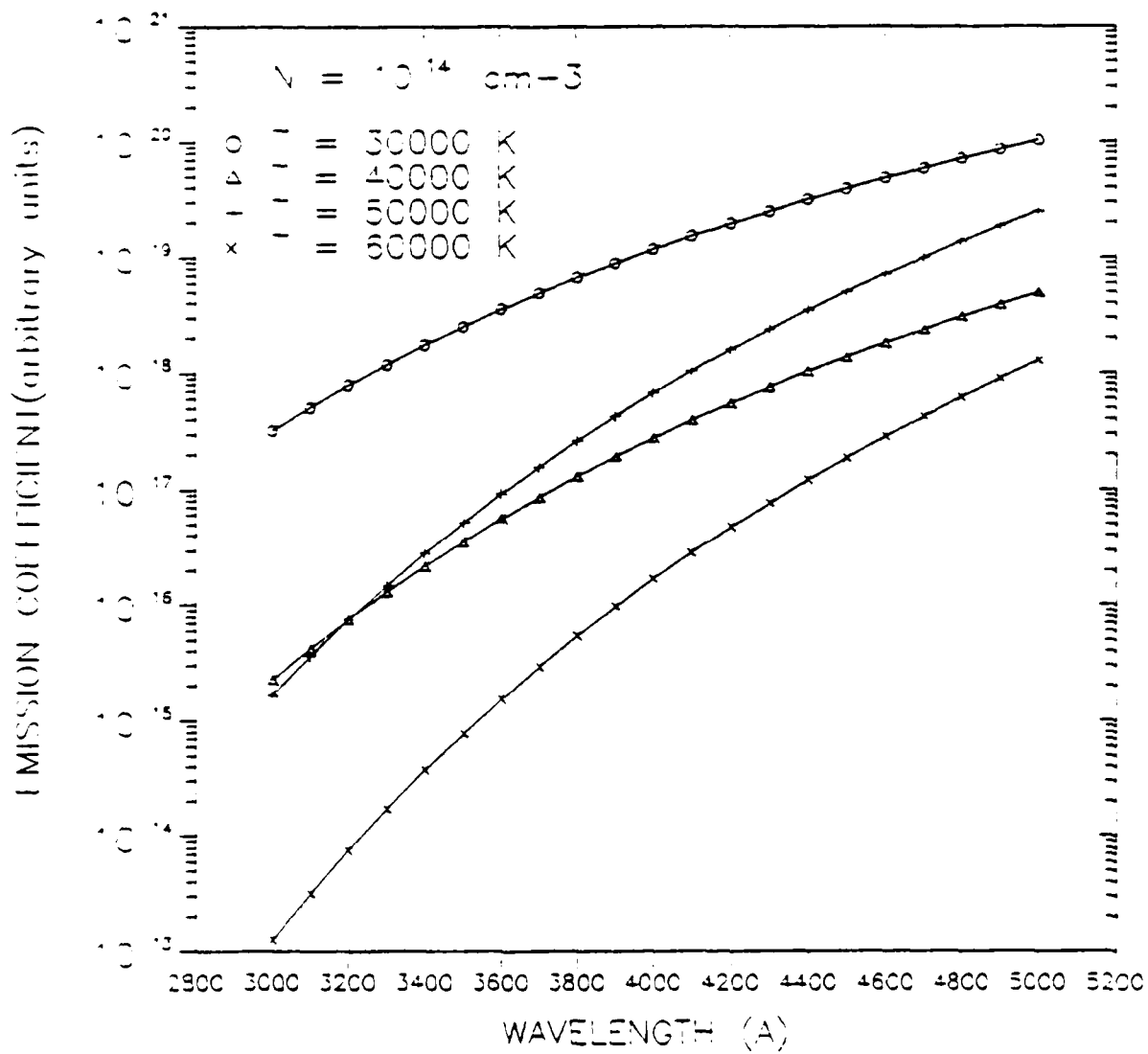


Fig. 13. Calculation of Emission Coefficients for Free-Free Transition in the Field of an Ion.

monochromator is $(\Omega/4\pi)N_p = (1/16f/\#^2)N_p$. Assuming that the loss of the grating is 18-25% and the loss of each mirror is 5-15%, the net radiance reaching the detector, N_{sp} , is

$$N_{sp} = R_{M1}R_{M2}R_G(\Omega/4\pi)N_p, \text{ where } R = \text{reflectance.}$$

$$\text{best case } N_{sp} = (0.95)^2(0.82)(\Omega/4\pi)N_p = 9.7 \times 10^{-4}N_p.$$

$$\text{worst case } N_{sp} = (0.85)^2(0.75)(\Omega/4\pi)N_p = 7.1 \times 10^{-4}N_p.$$

Thus, the amount of radiance after passing through the monochromator is ~1/1000 of the source radiance.

b. CVF

The CVF which we are considering consists of three 80# segments covering wavelengths from 2.5 to 14.5 μm . The front view[18] is shown in Fig. 14. Its specifications, which are valid for normal incidence and room temperature, are

	λ	D	t_{cvf}
Segment	Wavelength(μ)	Half-Bandwidth(%)	Peak Transmittance(%)
I	2.5-4.5 (SWIR)	<1.35	>25
II	4.4-8.0 (MWIR)	<1.35	>30
III	7.9-14.5(LWIR)	<1.8	>30

If we deviate from these conditions, typical wavelength shifts as a function of incident angle and temperature are shown in Figs. 15 and 16. From the half-bandwidth, we calculate the optimum resolution to be 0.05(SWIR), 0.08(MWIR), and 0.20(LWIR) μm .

The optimum angular slit width in degrees of a CVF, ϕ_{opt} , assuming a collimated and normal incidence beam, is[19]

$$\phi_{opt} = D \cdot H \cdot (\lambda / (\lambda_{max} - \lambda_{min}))$$

where D is the half-bandwidth and H is the angular length of linearity in degrees. Using the optimum slit width results in maximum energy throughput without loss in resolution. The ϕ_{opt} 's are shown in the following table:

MOUNTED 2.5-14.5 μ NARROW BANDPASS INFRARED
CIRCULAR VARIABLE FILTER SETS WCV-2.5/14.5-L

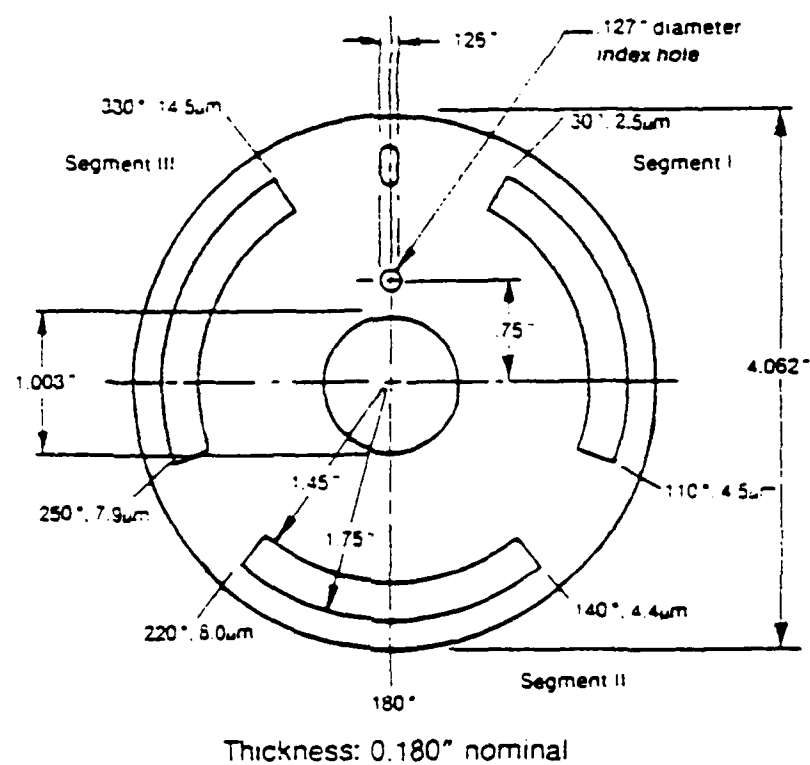


Fig. 14. Front View of CVF.

TYPICAL WAVELENGTH SHIFT OF INTERFERENCE FILTERS AS A FUNCTION OF ANGLE OF INCIDENCE COLLIMATED RADIATION

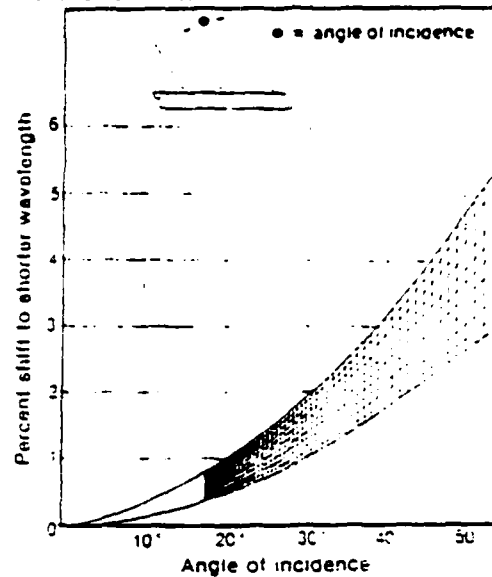


Fig. 15. Wavelength Shift of CVF as a Function of Incident Angle.

TYPICAL WAVELENGTH SHIFT AS A FUNCTION OF TEMPERATURE

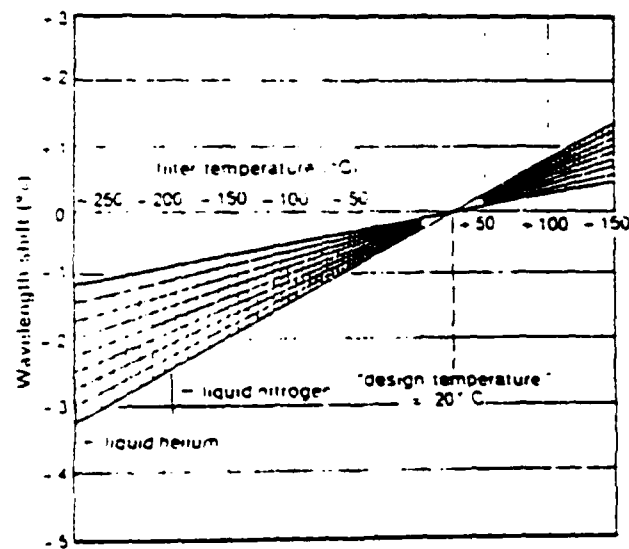


Fig. 16. Wavelength Shift of CVF as a Function of Temperature.

Segment	$\lambda(\mu)$	$\phi_{\text{opt}}(\text{deg})$
I	2.5	1.35
	3.5	1.89
	4.5	2.43
II	4.4	1.32
	6.2	1.86
	8.0	2.40
III	7.9	1.72
	11.2	2.44
	14.5	3.16

From the average angular slit width of 2.1° , the average linear slit width is calculated (assuming radius of 1.6") to be 1.5 mm. From Fig. 14 we can see that the useable slit height is 0.3". Thus the optimum useable area of the CVF with a rectangular slit is 0.11 cm^2 .

Two optical systems may be conceived to accommodate the CVF in the LINUS experiment. The first one is to use a single lens to focus the light onto the CVF (see Fig. 17). In order to avoid wavelength shift due to off angle incident beam, a f/8 or f/9 system is required. The net radiance in this case is

$$N_{\text{cvf}} = t_{\text{cvf}}(1/16f/\#^2)N_p \\ = 2\text{-}3 \times 10^{-4}N_p.$$

Thus this CVF arrangement has no advantage over the spectrometer.

The second arrangement is to use a fast lens, a collimator, and a slit (see Fig. 18). In this case the amount of light reaching the detector is

$$N_{\text{cvf}} = t_{\text{cvf}}R_c(1/16f/\#^2)(A_{\text{slit}}/A_{\text{collimator}})N_p.$$

If we place the collimator at a position such that its effective diameter is approximately the same as the slit height (7.62 mm), then the ratio, $A_{\text{slit}}/A_{\text{collimator}}$, is about 0.25 for 1.5 mm slit width. Assuming a f/1 lens and $R_c = 85\text{-}95\%$,

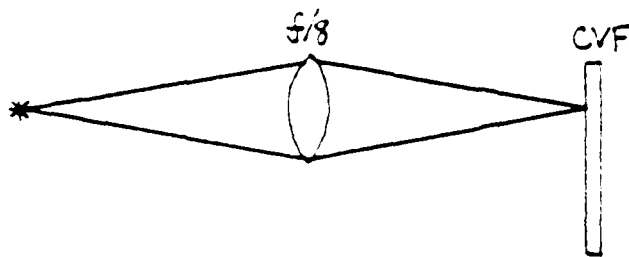


Fig. 17. Optical System Using One Lens for Using CVF in LINUS.

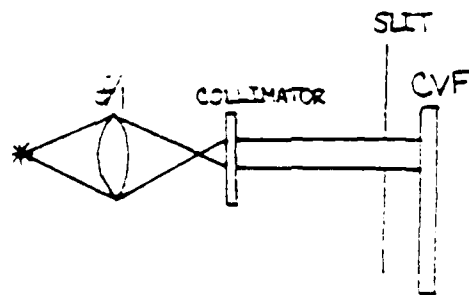


Fig. 18. Optical System Using Lens, Collimator, and Slit for Using CVF in LINUS.

$$N_{cvf} = 3.3-4.5 \times 10^{-3} N_p.$$

Thus if we use the optimum slit width, the gain of the CVF over the spectrometer is about a factor of 5 with a corresponding resolution loss of factors of 2(SWIR), 2(MWIR), and 5(LWIR). If we use the same slit width as the spectrometer, i.e. 3 mm, the gain of the CVF is approximately an order of magnitude, but with an even greater loss of resolution than above.

2. Net Throughput

The throughput, U , is defined as

$$U = A\Omega, \text{ where}$$

A = entrance aperture area

Ω = acceptance solid angle.

a. Spectrometer

The throughput of a grating spectrometer, U_{sp} , is

$$\begin{aligned} U_{sp} &= \text{slit area} * \text{acceptance solid angle} \\ &= h\Delta x(\pi/4f/\#^2) \end{aligned}$$

where h and Δx are the slit height and width respectively. With $h=0.2$ cm and $\Delta x=0.3$ cm, the throughput is $0.001 \text{ cm}^2\text{-sterad}$. Taking into account the loss on the three optical elements, the net throughput is

$$\begin{aligned} U_{sp}(\text{net}) &= (0.95)^2(0.82)(0.001) \\ &= 7.3 \times 10^{-4} \text{ cm}^2\text{-sterad}(\text{best case}). \\ U_{sp}(\text{net}) &= 5.4 \times 10^{-4} \text{ cm}^2\text{-sterad}(\text{worst case}). \end{aligned}$$

b. CVF

The throughput of a CVF is the same as that for an interferometer. This is given by

$$U_{cvf} = 2\pi A/R$$

where $R=\lambda/\Delta\lambda$ is the resolving power. The net throughput is

$$U_{\text{CVF}}(\text{net}) = t_{\text{CVF}}(2\pi A/R).$$

Using the optimum slit area of 0.11 cm^2 , the net throughput for the three segments is

Segment	$U_{\text{CVF}}(\text{net})(\text{cm}^2\text{-sterad})$
I	2.4×10^{-3}
II	2.8×10^{-3}
III	3.7×10^{-3}

The throughput of the CVF is about a factor of five higher than that of the spectrometer. If we use slit width of 3 mm, the throughput gain of the CVF is an order of magnitude. These results agree with the net radiance results. The comments on the resolution loss also apply.

From the above calculations we conclude that the CVF does have throughput advantage over the SPEX 1870 but this occurs only with a simultaneous reduction in resolution. Thus if one requires more throughput and if the resolution is not a critical factor in the experiment, then the CVF might be considered if a factor of 5-10 will be important.

3. Recommendations

The LINUS experiment might be improved upon by making the following two changes:

- Use a focusing lens which matches the $f/\#$ of the monochromator will help the light collection efficiency and permit the slit width to be reduced (discussed in more detail below).
- The focal waist of the focusing lens, r , is diffraction limited and is given by [20]

$$r = 1.22f\lambda/d.$$

Assuming properly matched optics, $r \approx 70 \text{ } \mu\text{m}$ at $\lambda = 8.5 \text{ } \mu\text{m}$. At present, a 3 mm slit width is used in the LINUS experiment which is much larger than the optimum slit width of $140 \text{ } \mu\text{m}$. Thus it might be worthwhile to close

down the slit to the position where the intensity begins to decrease in order to minimize scattered light.

VI. EXCEDE and ARCTIC

A. EXCEDE

We have acquired the EXCEDE[21] and ARCTIC[22,23,24] codes in order to pursue their applicability to the LABCEDE experiment.

Traditionally, energy deposition problems have been treated using the continuous slowing down approximation(CSDA), by solving the Fokker-Planck or Boltzmann equations, or doing a Monte Carlo calculation. The EXCEDE code (the special ARCTIC code which was applied to the EXCEDE project) employs a different theory of energy deposition to calculate energy deposition rate from which the radial distribution of electron density may be derived. This code was written by Tarr[21] and is important in its potential application to the LABCEDE electron scattering problem. The code was previously operated on the VAX 780 and we have been successful in converting it to run on the PC. Agreement between the results of a test case which ran on both computers is excellent. The theory is as follows.

If one starts with an electron beam incident on a gas, the code calculates the dynamics of electrons undergoing n number of collisions with the scattering gas. The parameters of interest are position(x), pathlength(l), energy(E), and angles of velocity vector (θ, ϕ). After n collisions the ensemble of electrons has a spread in the above parameters which may be represented by a probability distribution function, Z. If we know F, we can calculate quantities such as flux, Φ , energy deposition rate, $d\xi/dt$, and radial distribution of electron density, G(R). These are

$$\begin{aligned}\Phi &= J_0 \lambda \int F dl \\ d\xi/dt &= J_0 \lambda \int W F dl dE d\Omega \\ G(R) &= \int (d\xi/dt) dz\end{aligned}$$

where J = electron current density

λ = mean free path

W = probability that electron of energy E losing energy ϵ .

The code assumes a form for F and uses moments to define the assumed distribution. The moments are generated by differentiating the

characteristic functions of the random variables. To simplify the derivation of the equations, the assumption of many number of scattering events was made. It is this restriction which hinders the applicability of the code in its present form directly to the LABCEDE electron scattering problem because the LABCEDE experimental conditions give rise to only a few number of collisions. In order to apply the theory to the LABCEDE problem, the moment equations must be rederived without the assumption of many scattering events and the equations must be recoded.

Fig. 19 shows the output of the EXCEDE code for the case of 4.5 keV electrons and 10 collision events for N_2 gas. We see that the radial electron density has dropped by two orders of magnitude as the radius varies from 0 to 65 m. This is in vast contrast to experimentally obtained radial electron density in Fig. 20 which shows that the same drop occurs over a distance of 0.1 m[25]. This is not surprising from the discussion above. To apply the EXCEDE code to the electron scattering problem, we must rederive the set of moment equations without making the assumption of many number of scatterings.

B. ARCTIC

The ARCTIC code is a general purpose routine designed for calculating production rates and chemistry when a flux of auroral electrons bombards the atmosphere under ambient and disturbed conditions. The section on energy deposition is based on the electron energy loss program written by Peterson et al.[26]. The code is composed of a main driver program with 49 subroutines which control data input and output, and calculate volume production and emission rates. The code was originally programmed to run on the CDC 7600. Subsequently it was modified to run on the VAX 780. However, the core of the program remains in Fortran 66. This presents most of the problems when compiling the program on the PC(supports Fortran 77). Linktime errors arise from calling routines which are not supported on the PC. Runtime errors can be attributed to either the architecture of the PC or idiosyncrasies of the fortran compiler (IBM Professional Fortran).

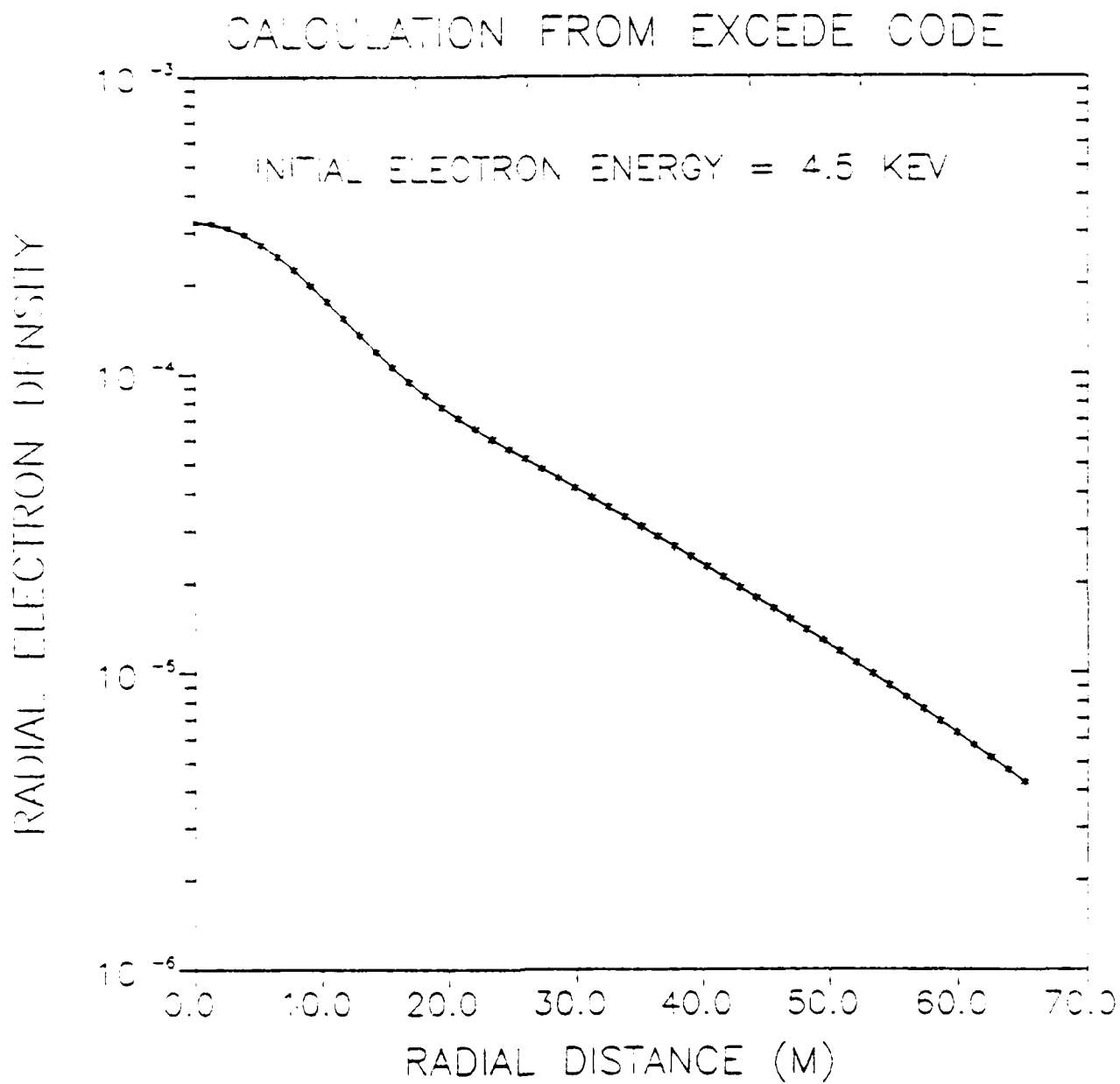


Fig. 19. EXCEDE Calculation for the Case of 4.5 eV Incident Electrons and 10 Collisions in N_2 .

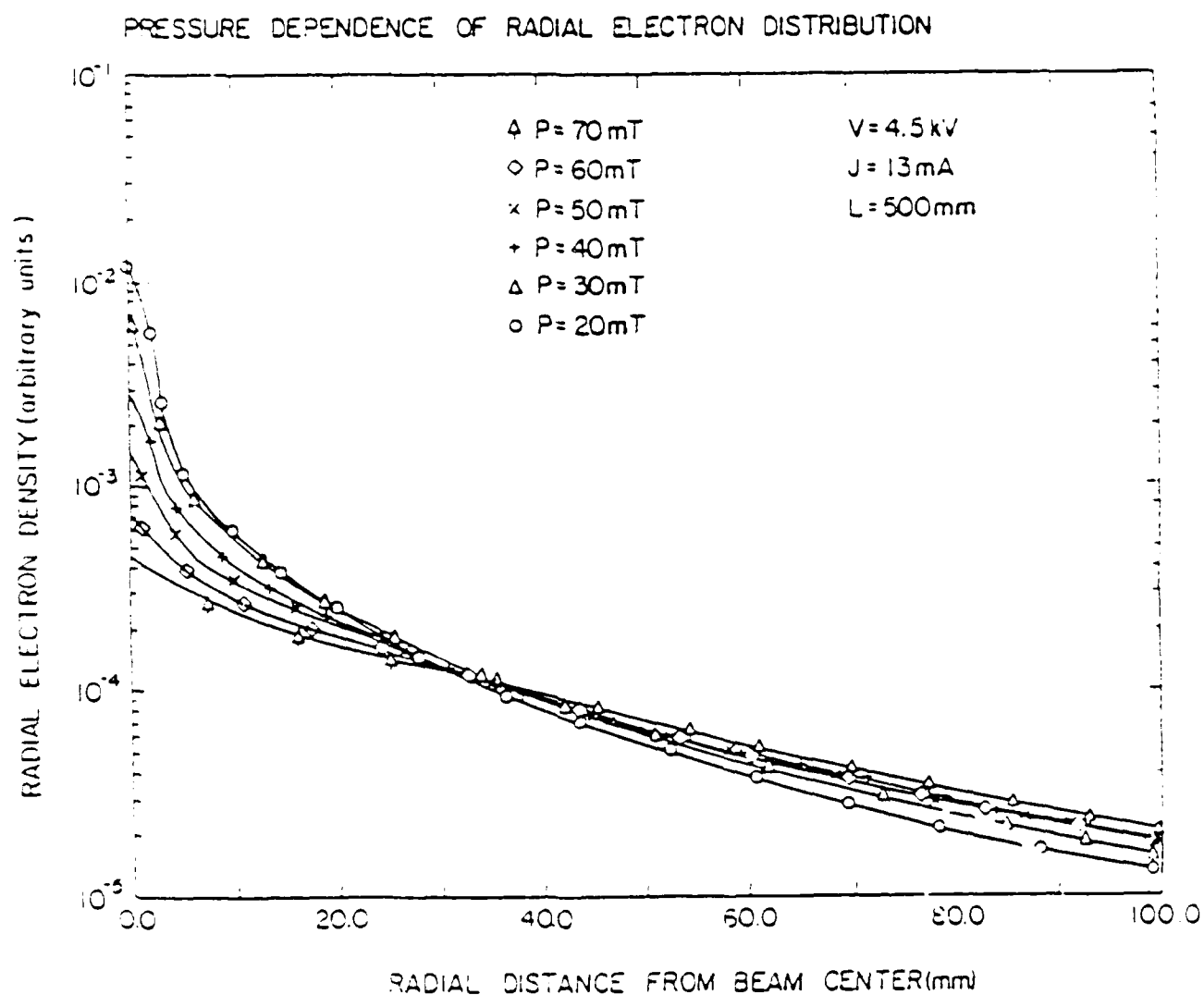


Fig. 20. Radial Electron Density Profiles in LABCEDE for 4.5 eV Incident Electrons in N_2 .

After making all the necessary changes, the program is tested by comparing to the results of a ELIAS drizzle case from the VAX. Agreement between the calculations using the two computers is excellent. Differences occur in the last decimal place, i.e. less than 1% error. On the VAX this problem typically takes ~2 hours to complete. On the XT, the production rates calculation takes ~21 hours and the chemistry code takes 1/2 to 1 hour per print time. On the COMPAQ 286, the running time reduces to 17 hours. The size of the executable version of the code is ~600 Kbytes which is just below the PC memory capacity of 640 K.

VII. REFERENCES

1. Sappenfield, D., "Radiation from a Recombining Oxygen Plasma", Los Alamos Supp. Rpt. LA-4303, 1971.
2. Blumberg, W.A.M., private communication, 1985.
3. Amsden, A.A., Ruppel, H.M., and Hirt, C.W., "SALE: A Simplified ALE Computer Program for Fluid Flow at All Speeds", LA-8095, 1980.
4. Armstrong, R.A., Lucht, R.A., and Rawlins, W.T., "Spectroscopic Investigation of Laser-Initiated Low-Pressure Plasmas in Atmospheric Gases". Appl. Opt. 22(10), 1573, 1983.
5. Armstrong, R.A., "Laser-induced Plasma Analysis", Mission Research Technical Report-MRC-NSH-R-0001, 1985.
6. Lurie, J.B. and Baird, J.C., "Short Wavelength Infrared Line Emission in a Laser Produced Oxygen Plasma". Chem Phys. Lett. 125, 389, 1986.
7. Dzelzkalns, L., private communication, 1986.
8. Wilke, M. and Stone, S., private communication to Kamegai, M., 1981.
9. Askar'yan, G.A., Rabinovich, M.S., Savchenko, M.M., and Stepanov, V.K., "Optical Breakdown "fireball" in the Focus of a Laser Beam", Soviet Phys. JETP Lett, 5, 121, 1967.
10. McLean, E.A., Stamper, J.A., Griem, H.R., Ali, A.W., Ripin, B.H., and Manka, C.K., "Spectroscopic Measurements of the Laser HANE Plasma", NRL-Memo-RPT-5 274, 1984.
11. Zel'dovich, Y.B., Raizer, Y.P., "Physics of Shock Waves and High Temperature Hydrodynamic Phenomena", Academic Press, 1966.
12. Sowle, D.H and Sappenfield, D.S., private communication.
13. Holland, D.H., Archer, D.H., Berkowitz, B.J., Hart, W.C., Hendrick, R.W. Jr., Humphrey, C., "Physics of High-Altitude Nuclear Burst Effects", MRC-R-30, 1977.
14. Dzelzkalns, L., Private communication, 1986.
15. Baird, J., private communication, 1986.
16. Morgan, C.G., "Laser-induced Breakdown of Gases", in "Electrical Breakdown of Gases", J.M. Meek & J.D. Craggs, eds., John Wiley & Sons, 1978.
17. Jenkins, F.A. and White, H.E., "Fundamentals of Optics", McGraw-Hill Book Co., 1957.

18. OCLI Infrared Stock Filter Catalog, January 1986.
19. OCLI paper - V.L. Yen, "Circular Variable Filters", reprinted from Optical Spectra, 3(3), P 78, 1969.
20. Halliday, D. and Resnick, R., "Physics", John Wiley & Sons, Inc., New York, 1962.
21. Tarr, P.W., "ARCTIC Code Electron Deposition Theory with Application to Project Excede", HAES Report No. 10, Mission Research Technical Report, MRC-R-173, 1975.
22. Archer, D.H. and Tarr, P.W., "Auroral Simulation Studies", HAES Report No. 6, Mission Research Technical Report, MRC-R-152, 1975.
23. Tarr, P.W. and Archer, D.H., "Auroral Simulation Studies in Support of ICECAP and EXCEDE", HAES Report No. 24, Mission Research Technical Report, MRC-R-211, 1975.
24. Archer, D.H. and Tarr, P.W., "Final Report on Auroral Simulation Effects", HAES Report No. 62, Mission Research Technical Report, MRC-R-313, 1977.
25. Ip, P.C.F., "Laboratory Studies of Electron Beam Growth in N_2 ", 1983-1984 AFGL-SCEEE Geophysics Scholar Program final report.
26. Peterson, L.R., Sawada, T., Bass, J.N., and Green, A.E.S., "Electron Energy Deposition in a Gaseous Mixture". Comp. Phys. Comm., 5, 239, 1973.

END

DATE
FILMED
5-88

DTIC